Numerical simulation of the wave-induced dynamic response of poro-elastoplastic seabed foundations and a composite breakwater

Jianhong Ye [a,b,c,*], Dongsheng Jeng [d], Wang Ren [a], Zhu Changqi [a]

[a] State Key Laboratory of Geomechanics and Geotechnical Engineering, Institute of Rock and Soil Mechanics, Chinese Academy of Sciences, Wuhan 430071, China
[b] Department of Civil and Environment Engineering, The Hong Kong University of Science and Technology, Clear Water Bay, Kowloon, Hong Kong
[c] Division of Civil Engineering, University of Dundee, Dundee DD1 4HN, UK
[d] Griffith School of Engineering, Griffith University, Gold Coast, Queensland 4222, Australia

ARTICLE INFO

ABSTRACT

In this study, an integrated numerical model FSSI-CAS 2D (previously known as POROWSSI 2D) is developed for the problem of wave-elasto-plastic seabed-structure interactions, where the Volume Average Reynolds Average Navier–Stokes (VARANS) equation is taken as the governing equation for wave motion and porous flow in porous medium; the dynamic Biot's equation known as "$u - p$" is taken as the governing equation for the dynamics of porous seabed soil under wave loading. The Pastor–Zienkiewicz Mark III proposed by Pastor et al. (1990) [45] is used to describe the dynamic behaviour of poro-elasto-plastic seabed under wave loading. This developed integrated numerical model is validated by a centrifuge test conducted by Sassa and Sekiguchi (1999) [30]. The developed integrated numerical model is applied to investigate the wave-induced dynamic response of a composite breakwater and its elasto-plastic seabed foundation. The numerical results indicate that the pore pressure in an elasto-plastic seabed builds up under wave loading, leading to the reduction of the contact effective stresses between soil particles. The residual liquefaction occurs when the effective stresses decrease to a value approaching zero. The wave-induced residual liquefaction in seabed is progressive downward. A parameter considering the cohesion and friction angle of soil is defined to evaluate the residual liquefaction potential. Analysis results illustrate that the friction angle of soil has significant effect on the soil liquefaction; and Nevada dense sand becomes liquefied if the defined parameter exceeded 0.86. Parametric study shows that wave characteristics and soil properties have significant effects on the wave-induced progressive residual liquefaction in loose elasto-plastic seabed foundation.

© 2014 Elsevier Inc. All rights reserved.

1. Introduction

In the last 20 years, numerous marine structures such as breakwaters, pipelines, turbines, and oil platforms have been widely constructed in offshore area to protect the coastline or port from erosion and damage, for fluid transport (petroleum, natural gas, or freshwater), to generate green energy, and for extracting crude oil from the seabed, respectively. However,

* Corresponding author at: State Key Laboratory of Geomechanics and Geotechnical Engineering, Institute of Rock and Soil Mechanics, Chinese Academy of Sciences, Wuhan 430071, China.
E-mail address: yejianhongcas@gmail.com (J. Ye).

these marine structures are vulnerable to wave-induced liquefaction in their seabed foundations because of excessive pore pressure. Some examples of breakwater failures have been reported in previous studies [1–9]. The main reason for the failure of breakwaters built on porous seabed in offshore areas is the lack of a good understanding of the wave–seabed structure interactions by the coastal engineers involved in the design and maintenance of marine structures.

According to Oumeraci [6], wave–structure interactions were always the key point addressed by engineers during the design of marine structures before the 1990s. Thus, the effect of the porous seabed on the stability of marine structures was not considered. Subsequently, the importance of the seabed foundations for a structure's stability was recognized gradually, where wave-induced liquefaction of the seabed foundations was frequently found to play a key role in the collapse of marine structures.

Since the 1990s, numerous studies have investigated wave–seabed structure interactions. The methods employed include analytical solutions, decoupled numerical models, and integrated numerical models. However, the analytical solutions can only deal with simple boundary conditions [10–13], e.g., the breakwater is normally simplified as a line without width and weight. In decoupled numerical models, the linear or nonlinear Stokes wave has generally been used to apply the wave-induced dynamic force that acts on the seabed and structures. Thus, the effects of the outer shapes of structures and the porosity of the seabed foundations on the wave field could not be considered using these approaches [14–16]. The integrated numerical model [17,18] can overcome the shortcomings of the decoupled models, where the Navier–Stokes equation governs the wave motion and the porous flow in the seabed, and Biot's equation governs the dynamics of the seabed soil. Thus, the effects of the outer shapes of marine structures and the porosity of the seabed foundations can be considered using these approaches. However, the complex wave motion in front of marine structures, such as breaking waves, cannot be modeled and the seabed foundations have been limited to poro-elasticity in previous investigations.

The soil types of the marine deposits found in offshore environment are generally sands, silts, and clays etc. Based on the deformation characteristics under external loading, the seabed soil can generally be classified into two types: elastic seabed and elastoplastic seabed. For elastic seabed soil, there is no unrecoverable deformation under external loading. Very dense marine deposited sand can be treated as an elastic seabed soil. The Quaternary newly deposited loose sand soil in offshore area is a typical elastoplastic soil. Normally, it has a low relative density D_r, S, and P wave speed, but a low standard penetration test (SPT) value. Its bearing capacity is generally weak and it readily liquefies under cyclic loading. Therefore, the elastoplastic seabed is generally not suitable for use as the foundations of marine structures. Under dynamic loading, such as seismic or wave loading, the soil particles of elastoplastic soils rearrange to reach their optimal potential arrangement (more dense), thereby leading to the compaction of the soil and pore pressure buildup. After long-term dynamic loading, the soil particles in elastoplastic seabed soil tend to make contact with each other in a dense manner, thereby reaching an optimum state. The relative density D_r, S, and P wave speed increase, whereas SPT value increases. Finally, under dynamic loading, the soil compaction due to plastic volumetric deformation is unlikely to occur again. In this situation, the seabed soil becomes an elastic porous medium. It should be mentioned that elastic and elastoplastic seabed soils are relative concepts because even the same seabed soils may be elastic or elastoplastic under different external loadings. The deformation characteristics of seabed soils depend on the soil properties, such as the particle size and relative density, as well as the characteristics of the external loading, such as its magnitude and application rate.

Corresponding to elastic and elasto-plastic seabed, there are two liquefaction mechanism: transient liquefaction and residual liquefaction, respectively. Transient liquefaction can only occur in an elastic seabed due to the phase lag of the wave-induced pore pressure in the elastic seabed. Normally, this appears periodically under a wave trough and it depends mainly on the permeability and saturation of the seabed soil. Residual liquefaction can only occur in an elastoplastic seabed due to the pore pressure buildup caused by the compaction of soil under cyclic wave loading. Residual liquefaction is the main risk for the stability of marine structures built on elastoplastic seabed foundations. Both types of liquefaction have been observed in laboratory tests and field trials [19–30].

Wave-induced transient liquefaction in an elastic seabed has been investigated widely in previous studies [31–35]. However, few investigations have addressed wave-induced residual liquefaction in an elastoplastic seabed. In addition, analytical approximation [36–38] and decoupled numerical models [39–44] were applied in previous studies. There is no an integrated numerical models have been developed for the interactions between waves, marine structures, and elastoplastic seabed foundations. As mentioned above, the elastoplastic seabed is not suitable for use as the foundations of marine structures due to its weak bearing capacity and residual liquefaction. However, coastal engineers have to cope with this situation if no other choice is available in specific working sites. Therefore, it would be useful to develop an integrated numerical model to evaluate the stability of marine structures built on elastoplastic seabed foundations under wave loading, which may help engineers to understand the mechanism of wave-elastoplastic seabed structure interaction.

In this study, an integrated numerical model is developed where the Volume Average Reynolds Average Navier–Stokes (VARANS) equation is used as the governing equation for wave motion and porous flow in a porous medium. In addition, the dynamic Biot's equation known as "$u - p$" is used as the governing equation for the dynamics of a porous seabed soil under wave loading. In this developed integrated model, the complex wave motion is modeled, which can consider the effects of the complex outer shapes of marine structures and the porous flow in an elastoplastic seabed on the wave field in front of marine structures. The acceleration of pore water and soil particles are both considered in the dynamic Biot's equation. This is essential for modeling the porous flow in a seabed with high porosity and permeability, such as a coarse sand bed. The Pastor–Zienkiewicz Mark-III (PZIII) constitutive model proposed by Pastor et al. [45] is used to describe the dynamic behavior of poro-elastoplastic seabed under wave loading. The integrated numerical model was validated using

a centrifuge test, which was conducted by Sassa and Sekiguchi [30]. Finally, the integrated numerical model was used to comprehensively investigate the wave-induced dynamic response of a composite breakwater and its elastoplastic seabed foundations. It should be noted that compressive stress is taken as a negative value in this study.

2. Integrated numerical model

2.1. Soil model

It is commonly known that soil is a multi-phase material, which comprises soil particles, water, and trapped air. In the soil mixture, the soil particles form the skeleton while the water and air fill the voids in the skeleton. Therefore, soil is a three-phase porous material, rather than a continuous medium. In the present study, the dynamic Biot's equations known as the "$u - p$" approximation, which was proposed by Zienkiewicz et al. [46], is used to govern the dynamic behaviors of a porous medium under wave loading, where the relative displacements of pore fluid to soil particles are apparently small for Darcy's laminar flow, thus they are ignored. However, the accelerations of the pore water and soil particles are included. The governing equations for a porous medium under a plain strain condition are

$$\frac{\partial \sigma'_x}{\partial x} + \frac{\partial \tau_{xz}}{\partial z} = -\frac{\partial p_s}{\partial x} + \rho \frac{\partial^2 u_s}{\partial t^2}, \tag{1}$$

$$\frac{\partial \tau_{xz}}{\partial x} + \frac{\partial \sigma'_z}{\partial z} + \rho g = -\frac{\partial p_s}{\partial z} + \rho \frac{\partial^2 w_s}{\partial t^2}, \tag{2}$$

$$k\nabla^2 p_s - \gamma_w n\beta \frac{\partial p_s}{\partial t} + k\rho_f \frac{\partial^2 \epsilon_v}{\partial t^2} = \gamma_w \frac{\partial \epsilon_v}{\partial t}, \tag{3}$$

where (u_s, w_s) = the soil displacements in the horizontal and vertical directions, respectively; n = soil porosity; σ'_x and σ'_z = effective normal stresses in the horizontal and vertical directions, respectively; τ_{xz} = shear stress; p_s = the pore water pressure; $\rho = \rho_f n + \rho_s(1 - n)$ is the average density of porous seabed; ρ_f = the fluid density; ρ_s = solid density; k = the Darcy's permeability; g = the gravitational acceleration; γ_ω is the unit weight of pore fluid; and ϵ_v is the volumetric strain. In Eq. (3), the compressibility of pore fluid (β) and the volume strain (ϵ_v) are defined as

$$\beta = \left(\frac{1}{K_f} + \frac{1 - S_r}{p_{w0}}\right), \quad \text{and} \quad \epsilon_v = \frac{\partial u_s}{\partial x} + \frac{\partial w_s}{\partial z}, \tag{4}$$

where S_r = the degree of saturation of seabed, p_{w0} = the absolute static pressure, and K_f = the bulk modulus of pore water. Based on the classic mechanical theory, the effective stresses in soil can be related to the displacements of soil by the following relationship

$$\begin{bmatrix} \sigma'_x \\ \sigma'_z \\ \tau_{xz} \end{bmatrix} = D \begin{bmatrix} \epsilon_x \\ \epsilon_z \\ \epsilon_{xz} \end{bmatrix} = D \begin{bmatrix} \frac{\partial u_s}{\partial x} \\ \frac{\partial w_s}{\partial z} \\ \frac{1}{2}\left(\frac{\partial u_s}{\partial z} + \frac{\partial w_s}{\partial x}\right) \end{bmatrix} \tag{5}$$

where ϵ_x, ϵ_z, and ϵ_{xz} are the three components of the strain of soil. D is the elastic matrix. Under plane strain conditions, the elastic matrix D can be expressed as

$$D = \frac{E}{(1 + v)(1 - 2v)} \begin{bmatrix} 1 - v & v & 0 \\ v & 1 - v & 0 \\ 0 & 0 & \frac{1-2v}{2} \end{bmatrix} \tag{6}$$

where E and v are the elastic modulus and Poisson's ratio, respectively. In this soil model, both elastic and elastoplastic models such as PZIII [45], Camb clay, and Mohr Column can be applied in the computations. If an elastoplastic constitutive model is used in the computation, the elastic matrix D should be replaced by an elastoplastic matrix D^{ep}

$$D^{ep}_{ijkl} = D^e_{ijkl} - \frac{D^e_{ijmn}m_{mn}n_{st}D^e_{stkl}}{H_{L/U} + n_{st}D^e_{stkl}m_{kl}} \tag{7}$$

where D^e_{ijkl} is the tensor form of the elastic matrix D, $H_{L/U}$ is the plastic modulus in the loading or unloading stage, m_{mn} is the plastic flow direction tensor, and n_{st} is the loading or unloading direction tensor. The above two direction tensors are formulated as:

$$m_{mn} = \frac{\left(\frac{\partial g}{\partial \sigma'_{mn}}\right)}{\left\|\frac{\partial g}{\partial \sigma'_{mn}}\right\|} \quad \text{and} \quad n_{st} = \frac{\left(\frac{\partial f}{\partial \sigma'_{st}}\right)}{\left\|\frac{\partial f}{\partial \sigma'_{st}}\right\|} \tag{8}$$

where $\left\|\frac{\partial g}{\partial \sigma'_{mn}}\right\|$ and $\left\|\frac{\partial f}{\partial \sigma'_{st}}\right\|$ represent the norm of the tensor $\frac{\partial g}{\partial \sigma'_{ij}}$ and $\frac{\partial f}{\partial \sigma'_{ij}}$, respectively. f and g are the yield surface function and plastic potential surface function in stress space, respectively. If the same function is used for both the yield surface f and the plastic potential surface g, then the associated flow rule will be applied, otherwise a non-associated flow rule will be applied.

The above governing equations for a porous medium are solved using a finite element method based on the geotechnical code SWANDYNE II platform, which was originally developed by Chan [47] for seismic wave-induced soil dynamics. To obtain the solution, the generalized Newmark-β method is used to determine the time integration. Further developments were made in the original code to include a loading modulus for various wave loadings and boundary conditions. Detailed information about discretization in the space domain and time domain can be found in [31,48,49].

In the present study, the elastoplastic constitutive model PZIII, which was proposed by Pastor et al. [45] based on the generalized plastic theory, is used to describe the mechanical behavior of sandy seabed foundations. In PZIII, the yield surface function f and the plastic potential surface function g, respectively, are defined as

$$f = q' - M_f p' \left(1 + \frac{1}{\alpha_f}\right) \left[1 - \left(\frac{p'}{p'_f}\right)^{\alpha_f}\right] = 0 \tag{9}$$

$$g = q' - M_g p' \left(1 + \frac{1}{\alpha_g}\right) \left[1 - \left(\frac{p'}{p'_g}\right)^{\alpha_g}\right] = 0 \tag{10}$$

In the loading and unloading stages, the plastic modulus is defined as:

$$H_L = H_0 p' \left(1 - \frac{q'/p'}{\eta_f}\right)^4 \left[1 - \frac{q'/p'}{M_g} + \beta_0 \beta_1 exp(-\beta_0 \xi)\right] \left(\frac{q/p'}{\eta_{max}}\right)^{-\gamma_{DM}} \tag{11}$$

$$H_U = \begin{cases} H_{u0} \left(\frac{M_g}{\eta_u}\right)^{\gamma_U} & \text{for } \left|\frac{M_g}{\eta_u}\right| > 1 \\ H_{u0} & \text{for } \left|\frac{M_g}{\eta_u}\right| \leqslant 1 \end{cases} \tag{12}$$

where p' and q' are the mean effective stress and deviatoric stress, respectively, and $M_f, M_g, \alpha_f, \alpha_g, \beta_0, \beta_1, \gamma$, and γ_{DM} are parameters used to describe the properties of sandy soil. Detailed information about the elastoplastic model PZIII can be found in Pastor et al. [45] and Zienkiewicz et al. [49]. PZIII is an excellent constitutive model for describing the behaviors of clay and sandy soils. Its reliability was validated based on a series of laboratory tests involving monotonic and cyclic loading [49]. This model is part of the heritage of Olek Zienkiewicz [50].

2.2. Wave model

The flow field inside and outside a porous medium is determined by solving the VARANS equations [51], which are derived by integrating the RANS equations over the control volume. The mass and momentum conservation equations can be expressed as:

$$\frac{\partial \langle \overline{u}_{fi} \rangle}{\partial x_i} = 0 \tag{13}$$

$$\frac{\partial \langle \overline{u}_{fi} \rangle}{\partial t} + \frac{\langle \overline{u}_{fj} \rangle}{n(1 + c_A)} \frac{\partial \langle \overline{u}_{fi} \rangle}{\partial x_j} = \frac{1}{1 + c_A} \left[-\frac{n}{\rho_f} \frac{\partial \langle \overline{p} \rangle^f}{\partial x_i} - \frac{\partial \langle \overline{u'_{fi} u'_{fj}} \rangle}{\partial x_j} + \frac{1}{\rho_f} \frac{\partial \langle \overline{\tau}_{ij} \rangle}{\partial x_j} + n g_i \right]$$

$$- \frac{\langle \overline{u}_i \rangle}{1 + c_A} \left[\frac{\alpha(1 - n)^2}{n^2 d_{50}^2} + \frac{\beta(1 - n)}{n^2 d_{50}} \sqrt{\langle \overline{u}_{f1} \rangle^2 + \langle \overline{u}_{f2} \rangle^2} \right] \tag{14}$$

where u_{fi} is the flow velocity, x_i is the Cartesian coordinate, t is time, ρ_f is the water density, p is pressure, τ_{ij} is the viscous stress tensor of the mean flow, g_i is the acceleration due to gravity, and n and d_{50} are the porosity and the equivalent mean diameter of the porous material, respectively. c_A denotes the added mass coefficient, which is calculated by $c_A = 0.34(1 - n)/n$. Based on the fitting and regression of a wide range of experimental data, Liu et al. [52] proposed the use of $\alpha = 200$ and $\beta = 1.1$ for a porous flow. Recently, Lara et al. [53] suggested two nonlinear relations between the empirical coefficients α and β, and the porosity n and mean particle size d_{50}: $\alpha = 4409.22 d_{50}, \beta = 12.27 \frac{n^3}{(1-n)^{1.5}} d_{50}^{-0.1075}$.

The influence of turbulence fluctuations on the mean flow, denoted as $\langle u'_{fi} u'_{fj} \rangle$, is obtained by solving the volume-averaged $k - \epsilon$ turbulence model. "$\langle \rangle$" and "$\langle \rangle^f$" denote Darcy's volume averaging operator and the intrinsic averaging operator, respectively, which are defined as:

$$\langle \overline{a} \rangle = \frac{1}{V} \int_{V_f} a \, dv, \quad \text{and} \quad \langle \overline{a} \rangle^f = \frac{1}{V_f} \int_{V_f} a \, dv \tag{15}$$

where V is the total averaging volume and V_f is the proportion of V that is occupied by the fluid. The relationship between Darcy's volume averaging operator and intrinsic volume averaging is: $\langle a \rangle = n \langle a \rangle^f$.

In the VARANS equations, the interfacial forces between the fluid and solids have been modeled according to the extended Forchheimer relationship, where both the linear and nonlinear drag forces between the pore water and the skeleton of the porous structure are included in the final term of Eq. (14). More detailed information about the RANS and VARANS models can be found in [54,51].

The volume-averaged $k - \epsilon$ equations for the volume-averaged turbulent kinetic energy k and the dissipation rate ϵ of the porous flow in porous structures, which are derived by taking the volume-average of the standard $k - \epsilon$ equations, are expressed as [51]:

$$\frac{\partial \langle k \rangle}{\partial t} + \frac{\langle \overline{u}_{fj} \rangle}{n} \frac{\partial \langle k \rangle}{\partial x_j} = \frac{\partial}{\partial x_j}\left[\left(\frac{\langle v_t \rangle}{\sigma_k} + v\right)\frac{\partial \langle k \rangle}{\partial x_j}\right] - \frac{\langle \overline{u'_{fi} u'_{fj}} \rangle}{n}\frac{\partial \langle \overline{u}_{fi} \rangle}{\partial x_j} - \langle \epsilon \rangle + n\epsilon_\infty \tag{16}$$

$$\frac{\partial \langle \epsilon \rangle}{\partial t} + \frac{\langle \overline{u}_{fj} \rangle}{n} \frac{\partial \epsilon}{\partial x_j} = \frac{\partial}{\partial x_j}\left[\left(\frac{\langle v_t \rangle}{\sigma_\epsilon} + v\right)\frac{\partial \epsilon}{\partial x_j}\right] - C_{1\epsilon}\frac{\langle \epsilon \rangle}{n\langle k \rangle}\langle \overline{u'_{fi} u'_{fj}} \rangle\frac{\partial \langle \overline{u}_{fi} \rangle}{\partial x_j} - C_{2\epsilon}\frac{\langle \epsilon \rangle^2}{\langle k \rangle} + nC_{2\epsilon}\frac{\epsilon_\infty^2}{k_\infty} \tag{17}$$

where v_t is the eddy viscosity. The empirical coefficients $C_{1\epsilon}, C_{2\epsilon}, \sigma_\epsilon$, and σ_k are set as 1.44, 1.92, 1.3, and 1.0, respectively, which were determined from stationary flow experiments [55]. In Eqs. (16) and (17), $\epsilon_\infty, k_\infty$, and $\langle v_t \rangle$ are defined as:

$$\epsilon_\infty = 39.0\frac{(1-n)^{2.5}}{n}(\langle \overline{u}_1 \rangle^2 + \langle \overline{u}_2 \rangle^2)^{1.5}\frac{1}{d_{50}} \tag{18}$$

$$k_\infty = 3.7\frac{1-n}{\sqrt{n}}(\langle \overline{u}_1 \rangle^2 + \langle \overline{u}_2 \rangle^2) \tag{19}$$

$$\langle v_t \rangle = C_\mu\frac{\langle k \rangle^2}{n\langle \epsilon \rangle} \tag{20}$$

where C_μ is a coefficient that depends on the local strain rate (see [51]).

In the wave model, the finite difference two-step projection method on a staggered grid system is used for space discretization and the forward time difference method is used for the time derivative. The VOF method is applied to track the water free-surface. The combined central different method and upwind method are used to solve the $k - \epsilon$ equations. More detailed information can be found in Lin [56] and Hsu et al. [51]. The above VARANS equations and $k - \epsilon$ equations are solved using the N-S solver in COBRAS.

In this wave model, the internal wave maker proposed by Lin and Liu [57] is used to generate the target wave train, where a mass function is added to the continuity equation. Various waves could be generated by applying different mass functions, e.g., linear wave, solitary wave, 2nd-order and 5th-order Stokes wave, and cnoidal wave. If the steepness of the generated wave reaches a certain value, the wave will break while propagating on the seabed.

2.3. Integrated method

In the coupling computation, the wave model is responsible for the generation, wave propagation, and porous flow in porous media (seabed, rubble mound, breakwater, etc.), and it determines the pressure that acts on the seabed and marine structures. The VARANS equations are fully coupled at the interfaces between the fluid domain and the porous medium via the pressure and velocity/flux continuity, thus the pressure and flow field are continuous in the whole computational domain. At the same time, the pressure/force that acts on the seabed and marine structures, which is determined by the wave model, is provided to the soil model via a data exchange port that was developed to calculate the dynamic response
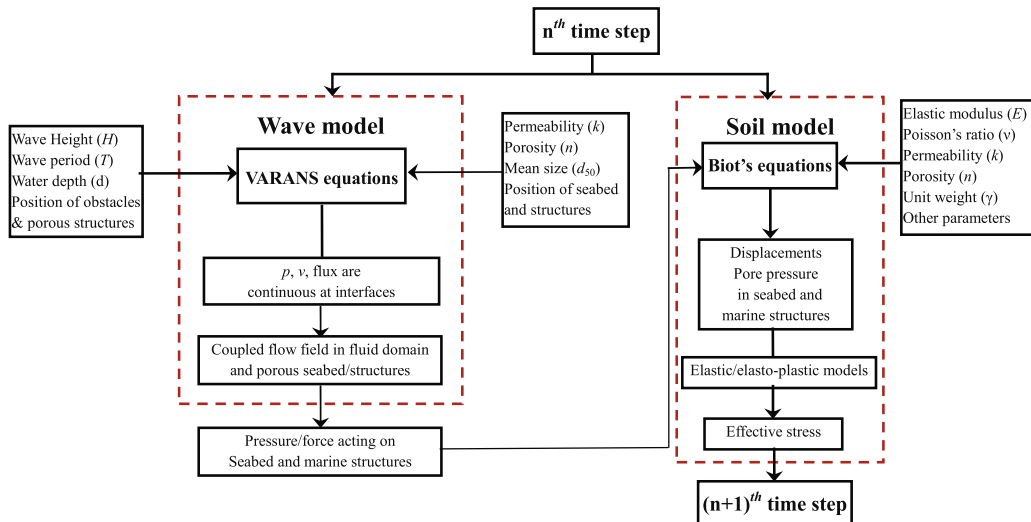
Fig. 1. Coupling process employed in FSSI-CAS 2D.

of seabed and marine structures, including the displacements, pore pressure, and effective stresses. The coupling process is illustrated in Fig. 1. More information about the data exchange port can be found in [31].

3. Verification of the integrated model

The integrated model FSSI-CAS 2D has been validated based on analytical solutions and in a series of laboratory wave flume tests with respect to the problem of wave-elastic seabed or wave-marine structure-elastic seabed foundations interactions [31]. However, the suitability of the integrated model FSSI-CAS 2D for wave-elastoplastic seabed interactions has not been validated previously. In this section, the centrifuge test described by [30] is used to validate the integrated model FSSI-CAS 2D with respect to the wave-elastoplastic seabed interaction problem. This verification was also published recently [58]. However, to ensure the completeness of the present study, we describe this verification process again, as follows.

Sassa and Sekiguchi [30] conducted a series of centrifuge tests to investigate wave-induced liquefaction in a sandy bed. A wave paddle was installed in a container to generate a wave that propagated to the sandy bed. The experimental set up is shown in Fig. 2. The sand used in the tests was Leighton Buzzard sand (British Standard sieve 100/170). The physical properties of the sand were: specific gravity G_s = 2.65, mean grain size d_{50} = 0.15 mm, maximum void ratio e_{max} = 1.07, and minimum void ratio e_{min} = 0.64. Test P5-1 was used in the verification performed in this study. In test P5-1, a progressive wave was generated by the wave paddle. The wave characteristics were: water depth = 90 mm, wave period = 0.09 s, wave height = 32 mm (thus the amplitude of the wave-induced pressure acting on the sandy bed was 5.0 kPa). The relative density of the sand in the container was D_r = 42%. The test was performed under an acceleration of 50g because the viscosity of the silicone oil used in the centrifuge test was 50 times that of water. According to the scaling principle, the wave modeled in the centrifuge test was equivalent to a wave with: water depth = 4.5 m, wave period = 4.5 s, and wave height = 1.6 m; and the length and height of the sandy bed in the centrifuge test were equivalent to 10 m and 5 m, respectively, when the acceleration was 1g. During testing, the pore pressure were measured for four typical points at depths of 0 mm, −10 mm, −40 mm, and −91 mm in the midline of the sandy bed (see Fig. 2). Based on a range of parametric finite elements (FE) analyses and by comparing the numerical results with the centrifuge test results, the parameters of the sand were successfully identified for the PZIII model, as described by Sassa and Sekiguchi [43]. All of the parameters used in the verification computation are listed in Table 1.

The integrated model FSSI-CAS 2D was used to simulate the wave-induced liquefaction that occurred in the centrifuge test based on the parameters listed in Table 1 and the aforementioned wave characteristics. The wave model in FSSI-CAS 2D was used to generate the expected wave in the container and the soil model in FSSI-CAS 2D was used to determine the wave-induced dynamics and the liquefaction of the sandy bed. During the computation, the PZIII model was used to describe the behavior of the sandy bed.

Fig. 3 compares the wave-induced excess pore pressure in the sandy bed based on the numerical results determined by FSSI-CAS 2D and the experimental data measured in the centrifuge test, according to Sassa and Sekiguchi [30]. Fig. 3 shows that the agreement between the numerical results and the experimental data is very high. This indicates that the integrated model FSSI-CAS 2D is suitable for the wave-elastoplastic seabed interaction problem.

4. Boundary conditions

The Computational domain is shown in Fig. 4. The seabed foundations include a flat part (−300 m−−100 m) and a sloped part (−100 m–550 m). The thickness of the flat part is 20 m. The gradient of the sloped part of the seabed foundations is 2:100. The composite breakwater is built on the sloped seabed (200 m–236 m). The dimensions of the composite breakwater
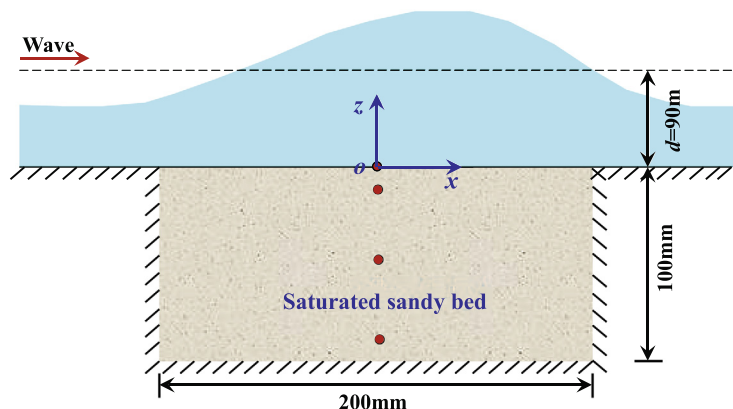
Fig. 2. Experimental setup of the centrifuge test conducted by [30].

Table 1
Parameters of the sandy soil used in [30] for the PZIII model.

Parameters	Value	Unit
K_{evo}	1517	[kPa]
G_{eso}	2100	[kPa]
p'_0	72.25	[kPa]
M_g	0.7	–
M_f	0.46	–
α_f	0.01	–
α_g	0.01	–
β_0	0.2	–
β_1	2.5	–
H_0	700	[kPa]
H_{U0}	1000	[kPa]
γ_u	6.0	–
γ_{DM}	4.0	–
Poisson's ratio (v)	0.3	–
Relative density (D_r)	42%	
Porosity (n)	0.445	
Permeability (k)	1.5×10^{-4}	[m/s]
Saturation (S_r)	100	%

are shown in Fig. 4. The water depth on the flat seabed foundations is 15 m. In the numerical calculations, the following boundary conditions are applied:

(1) The bottom of the seabed foundations is treated as rigid and impermeable.

$$u_s = w_s = 0 \quad \text{and} \quad \frac{\partial p_s}{\partial z} = 0 \quad \text{at } z = 0m \tag{21}$$

(2) The two lateral sides of the computational domain are fixed in the horizontal direction.

$$u_s = 0 \quad \text{at } x = -300 \text{ m} \quad \text{and} \quad x = 550 \text{ m} \tag{22}$$

(3) The surface of the seabed foundations and the composite breakwater can move freely. However, the pressure, including the hydrostatic pressure and wave-induced dynamic pressure, is applied to the surface of the seabed and the outer surface of the composite breakwater. In this study, the pressure is determined by the wave model. The pressure is applied to the seabed surface and outer surface of the composite breakwater via the data exchange port.
(4) The caisson is generally concrete, thus its permeability is small. In this study, the caisson is treated as an impermeable material during computations. The upward floating force that acts on the bottom of the caisson is taken into consideration in the computations. Otherwise, the initial effective stresses in the seabed foundations beneath the composite breakwater and the settlement of the composite breakwater are overestimated significantly.

5. Results and discussion

This section investigates the dynamic response of the composite breakwater and its poro-elastoplastic seabed foundations under wave loading using the integrated model FSSI-CAS 2D. In the computations, the composite breakwater is treated as an elastic medium. The elastoplastic soil constitutive model PZIII is adopted for the porous seabed. In total, 16065 four-node iso-parametric elements are used to discretize the computational domain. The slip elements are used to simulate the contact effect at the interfaces between the caisson and rubble mound, as well as between the rubble mound and seabed foundations. The property parameters for the poro-elastoplastic seabed are the same as those used in Zienkiewicz et al. [49], which were determined based on a series of tests using Nevada dense sand and Nevada fine sand in the VELCAS project. All of the properties of the seabed and composite breakwater are listed in Table 2. In the parametric study, the standard parameters for soil and ocean wave are: $k = 1.0 \times 10^{-5}$ m/s, $S_r = 98\%$, $H = 3.0$ m, $T = 8.0$ s.

5.1. Consolidation

In a real offshore environment, the seabed foundations have generally experienced a consolidation process due to hydrostatic pressure and self-gravity throughout its geological history. Thus, there is no excess pore pressure in the seabed foundations. In practical engineering, after the construction of a composite breakwater on the seabed foundations, the seabed beneath and close to the composite breakwater is compressed by the weight of the composite breakwater. This compression generates excess pore pressure in the seabed foundations during the early stage. As time passes, the excess pore pressure in the seabed foundations dissipates gradually, while the composite breakwater subsides downward. Finally, the seabed foundations reach a new consolidation state under the seawater and composite breakwater loading. In this study, the consolida-
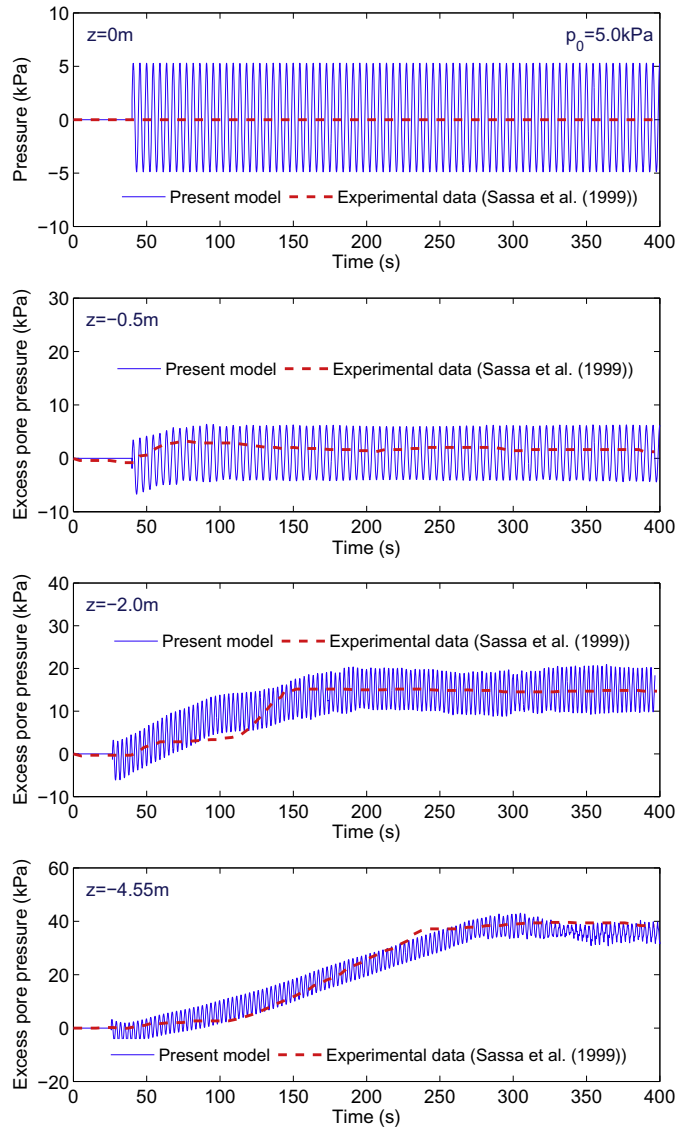
Fig. 3. Comparison of the excess pore pressure in a sandy bed based on the numerical results determined using the proposed model and the experimental data measured by [30]. Note that only the residual pore pressure is shown for the experimental data, whereas both the residual and oscillatory pore pressure are shown for the numerical results. The depths of the four monitoring points on the middle line are scaled up by 50 times.
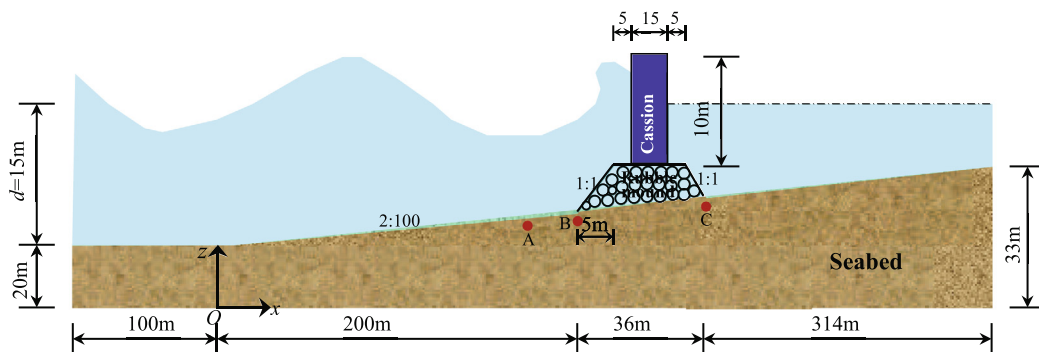
Fig. 4. Schematic graph of the computational domain addressed in this study, where a composite breakwater is built on the sloped seabed foundations [31].

Table 2

Properties and parameters used for the seabed foundations, composite breakwater, and wave in the analysis and parametric study.

Iterm	Nevada dense sand		Unit
Parameters for PZ3 model (Nevada sand)			
K_{evo}	2000		[kPa]
G_{eso}	2600		[kPa]
p'_0	4		[kPa]
M_g	1.32		–
M_f	1.3		–
α_f	0.45		–
α_g	0.45		–
β_0	4.2		–
β_1	0.2		–
H_0	750		–
H_{U0}	40,000		[kPa]
γ_u	2.0		–
γ_{DM}	4.0		–
Soil characteristics			
Permeability	1.0×10^{-2}, 1.0×10^{-5} or 1.0×10^{-7}		[m/s]
Poisson's ratio	0.3333		
Saturation	95, 98 or 100		%
Porosity	0.25		
Breakwater			
	Caisson	Rubble mound	
Permeability	1.0×10^{-10}	2.0×10^{-1}	[m/s]
Poisson's ratio	0.25	0.3333	
Saturation	0	99	%
Young's modulus	1.0×10^4	1.0×10^3	[MPa]
Porosity	0.1	0.35	
Wave characteristics			
Wave height		2.0, 3.0, 4.0	[m]
Wave period		6.0, 8.0, 10.0	[s]
Water depth		15	[m]

tion state of the seabed foundations under hydrostatic pressure and the weight of the composite breakwater is determined first to simulate the interaction between the ocean waves, seabed, and marine structures as accurately as possible. This consolidation state is then used as the initial condition for the analysis of the dynamic response of the seabed foundations under ocean wave loading.

Fig. 5 shows the pore pressure distribution after the construction of the composite breakwater, as well as the pore pressure distribution and initial effective stresses in the seabed foundations in the final consolidation status under hydrostatic pressure and the weight of the composite breakwater loading. It should noted that only the results between x = 0–350 m are shown. As illustrated in Fig. 5, the excess pore pressure is generated in the seabed foundations during the early stage after the construction of the composite breakwater. The maximum pore pressure reaches 460 kPa at the bottom of seabed, which is significantly greater than that (340 kPa) in the final consolidation state. It can also be seen that the initial stress fields are affected greatly by the composite breakwater. The initial horizontal and vertical effective stresses σ'_x and σ'_z both increase greatly in the zone beneath the composite breakwater. The distribution of shear stress τ_{xz} shows that there are two shear stress concentration zones in the region under the composite breakwater. The magnitude of shear stress reaches 20–30 MPa. This may be a direct explanation for shear failure in the seabed foundations.

Fig. 6 shows the distribution of the displacements of the seabed foundations and composite breakwater in the final consolidation state. After the composite breakwater is constructed on the seabed, the seabed foundations move toward two lateral sides and subside downward due to the compression of the composite breakwater. The final settlement of the composite breakwater is 70–80 mm, which is much greater than the horizontal displacement of only about 2–4 mm. More detailed discussions of the consolidation of the seabed foundations under a breakwater can be found in [59,60].

5.2. Wave field in front of the composite breakwater

The wave model in FSSI-CAS 2D is used to govern the generation, propagation of waves on the porous seabed, and the interaction with the seabed foundations and marine structures. In this study, the seabed foundations and rubble mound are treated as permeable media. Thus, there is fluid exchange between the seawater and the pore water in the seabed foundations or rubble mound at their interfaces. The caisson is generally made of concrete, thus it is treated as an impermeable structure that rests on the rubble mound.
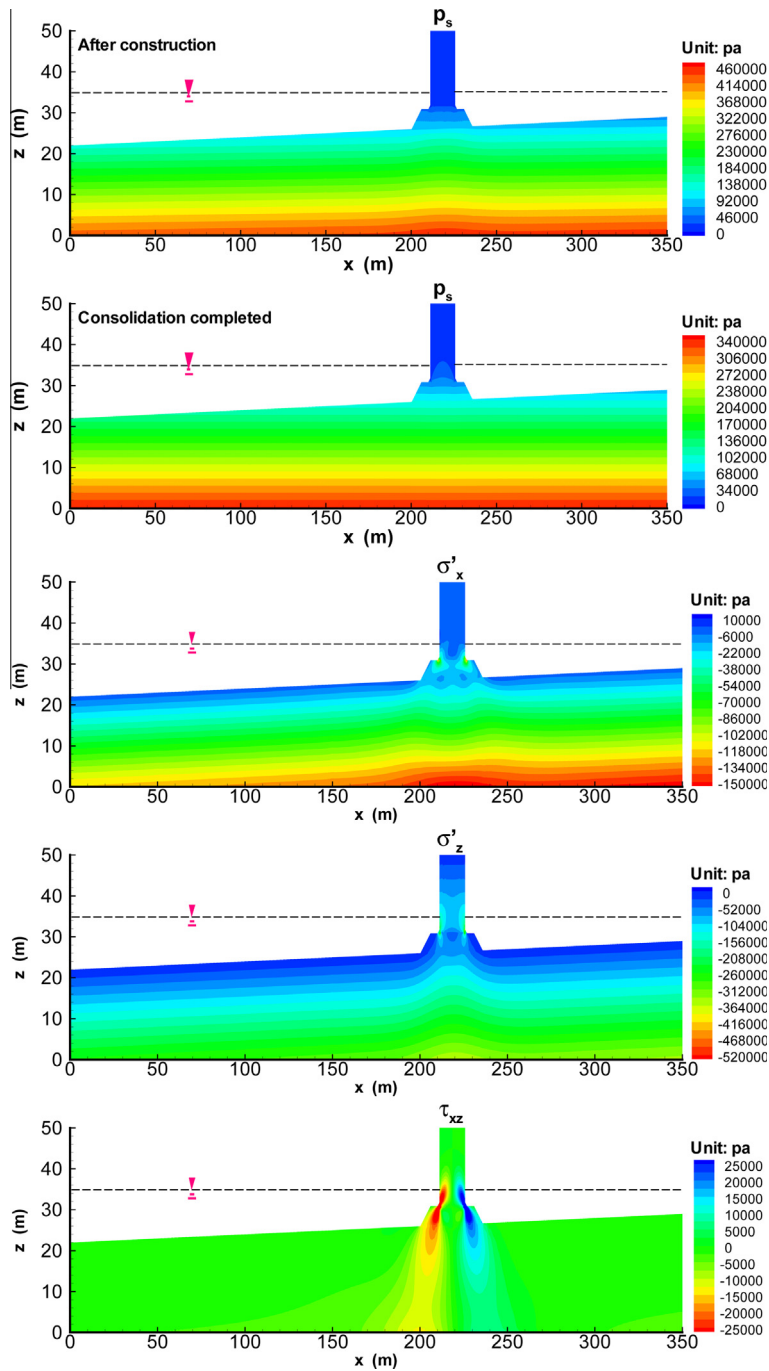
Fig. 5. Distribution of pore pressure in the seabed foundations after the construction of a composite breakwater, and the distribution of the pore pressure and the initial effective stresses in the seabed foundations in the final consolidation state.

Fig. 7 is a typical graph showing the interaction between the ocean waves, seabed, and composite breakwater at time $t = 250$ s. In the wave model, a wave maker is placed over the flat part of the seabed foundations. The ocean wave is generated by the wave maker with: wave height $H = 3$ m, period $T = 8$ s, and water depth $d = 15$ m. After being generated successfully, the ocean wave propagates to the composite breakwater. The sloped seabed foundations make the water depth decrease gradually, thus the wave characteristics on the sloped seabed foundations differ according to the wave conditions employed by the wave maker. The wave height increases as the wave length decreases. Furthermore, wave damping also exists because of the porous seabed. When the wave arrives at the composite breakwater, the wave is reflected partly.
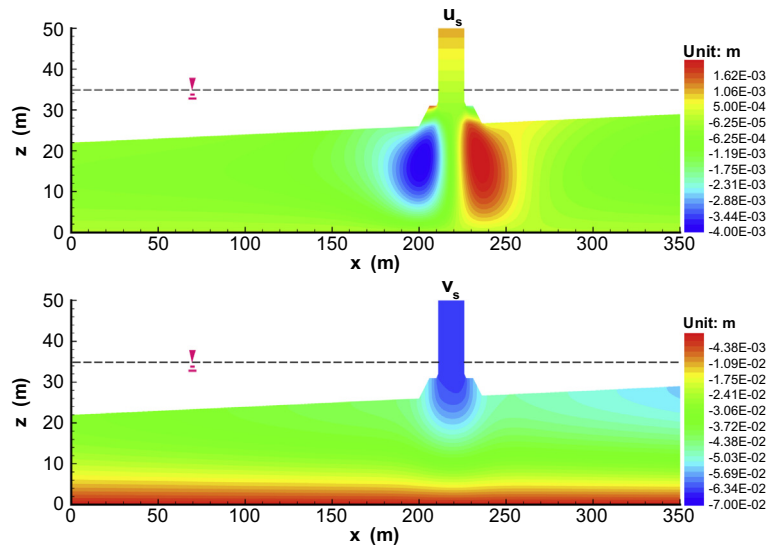
Fig. 6. Distribution of the initial displacement fields in the seabed foundations in the final consolidation state.
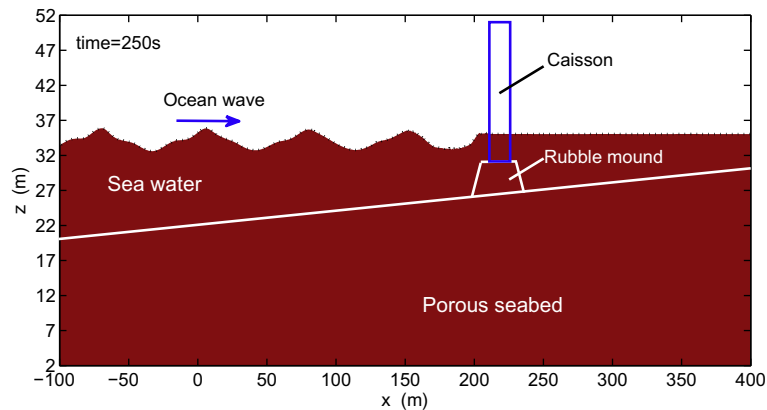
Fig. 7. Wave profile in front of the composite breakwater at time t = 250 s (H = 3 m, T = 8 s, d = 15 m) [31].

The reflected wave interferes with the incident wave in front of the composite breakwater, thereby making the wave height almost double the original wave height. Another small part of the wave energy drives the pore water to pass through the rubble mound. The wave energy is dampened during the process of propagation and interaction with the porous seabed and marine structures. It should be noted that the interaction between the waves, porous seabed, and rubble mound are not considered fully in the wave model, where the flow field of the seawater and pore water in the seabed and rubble mound is a fully coupled field.

5.3. Dynamic response of the composite breakwater and seabed foundations

In the coupling analysis, to investigate the dynamic response of the composite breakwater and poro-elastoplastic seabed foundation, the pressures acting on the seabed foundations and composite breakwater, which are determined by the wave model, are applied to the soil model as boundary conditions.

Fig. 8 shows the displacements of the caisson during the wave, seabed foundations, and composite breakwater interactions. The results shown are based on an elastic seabed and an elastoplastic seabed. It is clear that the displacements of the caisson are completely different with elastic and elastoplastic seabed foundations. With elastic seabed foundations, the caisson fluctuates periodically under the wave loading based on the original position determined in the final consolidation state. With elastoplastic seabed foundations, however, the caisson moves continuously toward the left and downward, which indicates that the elastoplastic seabed foundations are softening under the wave loading. In addition, the tilting of the caisson to the left-hand side does not tend to converge. During the later stage of wave loading, the rate of caisson tilting becomes
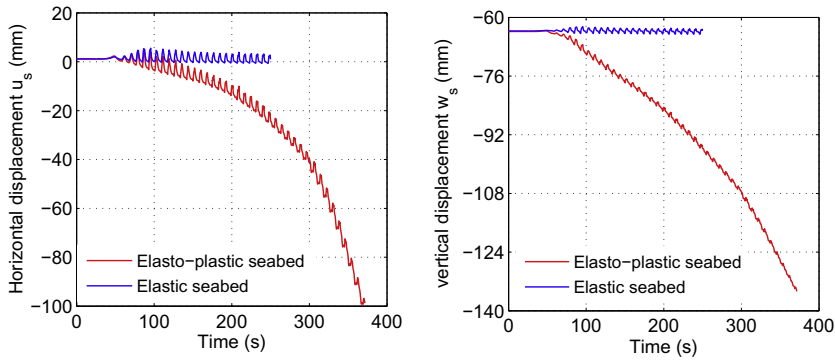
Fig. 8. Horizontal and vertical displacements of the caisson under the wave loading.

increasingly faster and the composite breakwater tends to collapse. This may be attributed to irreversible plastic volumetric deformation and the built-up of pore pressure in the seabed foundation. Under the wave cyclic loading, re-arrangement of the soil particles occurs in the poro-elastoplastic seabed, where the compaction of the sandy soil makes the pore pressure build up. This reduces the effective stresses between the soil particles. The reduction in the effective stresses directly makes the stiffness of the seabed foundation decrease significantly. The bearing capacity of the seabed foundations is also reduced accordingly. When the wave-induced excess pore pressure in the seabed foundations is sufficiently large, thereby making the effective contact stress equal to 0 (known as liquefaction), the seabed foundations lose their bearing capacity completely and they behave like a liquid. At this point, the composite breakwater will collapse. With elastic seabed foundations, there is no buildup of pore pressure under wave loading and the composite breakwater can only fluctuate periodically.

Figs. 9–11 illustrate the pore pressure build up process, with effective stress reduction at three typical positions: A ($x = 170$ m, $z = 22.9$ m), B ($x = 200$ m, $z = 23.5$ m), and C ($x = 236$ m, $z = 24.2$ m). The three figures show that the pore pressure in the seabed foundations has two components: oscillatory pore pressure and residual pore pressure. The residual pore pressure reduces the effective stresses between the soil particles and the oscillatory pore pressure makes the effective stresses oscillate accordingly. In Fig. 9, it can be seen that the wave-induced residual pore pressure cannot build up continuously, thus it remains almost constant after many cycles of wave loading. It can also be seen that the magnitudes of the effective stresses σ'_x and σ'_z decrease gradually during pore pressure build up. At time $t = 250$ s, σ'_x and σ'_z are almost 0. This indicates that position A ($x = 170$ m, $z = 22.9$ m) is basically liquefied at time $t = 250$ s under the wave loading. Another interesting
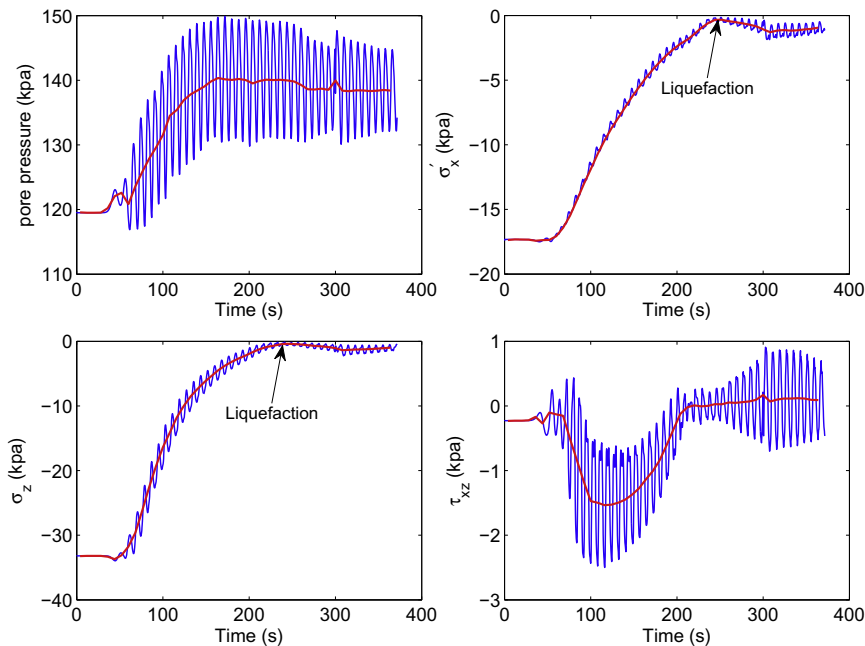
Fig. 9. Build up of the pore pressure and reduction of the effective stresses in the seabed foundations at position A ($x = 170$ m, $z = 22.9$ m), located on the left side of the composite breakwater.
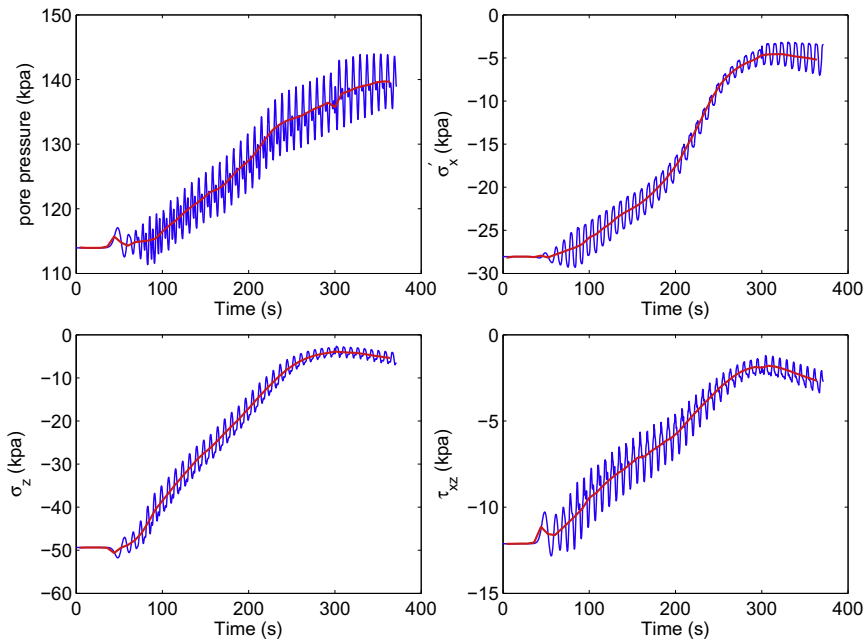
Fig. 10. Build up of the pore pressure and reduction of the effective stresses in the seabed foundations at position B ($x = 200$ m,$z = 23.5$ m), located under the left foot of the composite breakwater.
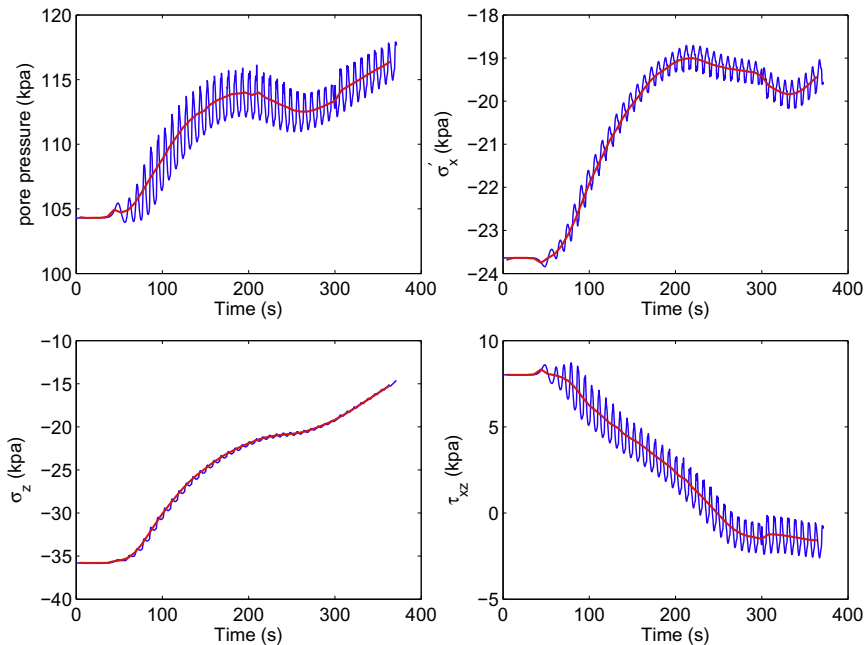
Fig. 11. Build up of the pore pressure and reduction of the effective stresses in the seabed foundations at position C ($x = 236$ m,$z = 24.2$ m), located under the right foot of the composite breakwater.

phenomenon is that the shear stress τ_{xz} is also almost 0 during the later stage of wave loading. This indicates that the effective contact stresses between the soil particles in the almost liquefied soil are very small. Naturally, an almost liquefied soil cannot bear a large shear stress. The fluctuation of the shear stress τ_{xz} is attributable to the wave-induced oscillatory pore pressure.

Fig. 10 shows that the magnitudes of the effective stresses σ_x', σ_z', and τ_{xz} all decrease during pore pressure build up. However, σ_x', σ_z', and τ_{xz} all do not approach 0, which indicates that position B ($x = 200$ m,$z = 23.5$ m) does not liquefy under the

wave loading. These findings differ from those at position A ($x = 170$ m, $z = 22.9$ m). This is mainly because the stress status at position B ($x = 200$ m, $z = 23.5$ m), which is under the left foot of the composite breakwater, is affected significantly by the gravity of the composite breakwater. The gravity of the composite breakwater compresses the seabed foundation, thereby greatly increasing the effective stresses in the underlying zone in the initial consolidation state. Under the wave loading, the compression of the composite breakwater makes it more difficult for the effective contact stresses in the seabed foundations to reach zero.

Fig. 11 shows the pore pressure buildup at position C ($x = 236$ m, $z = 24.2$ m), which is under the right foot of the composite breakwater. Position C ($x = 236$ m, $z = 24.2$ m) is located at the right-hand side of the caisson, but there is no direct wave loading on the seabed surface and the pore pressure still builds up. This can be attributed to the dissipation of the excess pore pressure in the seabed foundation from a high pressure zone to a low pressure zone. Under the wave loading, the pore pressure in the left part of seabed is much higher than that in the right part of the seabed. The pore water permeates the seabed foundation from the left-hand side of the composite breakwater to the right-hand side. This leads directly to the generation of excess pore pressure in the zone located at the right-hand side of the composite breakwater. However, the range of influence is limited on the right-hand side of the seabed foundation (see the distribution of p_s in Fig. 16). σ_x', σ_z' also fail to approach 0 during the later stage of wave loading (far from liquefaction). It is interesting to note that the shear stress τ_{xz} changes its direction (from positive to negative) at about $t = 240$ s. This may be due to the excessive tilting of the composite breakwater under the wave loading.

As mentioned above, the pore pressure in the seabed foundations comprises oscillatory pore pressure and residual pore pressure. It is useful to consider the distribution of the two types of pore pressure along the depth of the seabed foundation. Fig. 12 shows the distribution of oscillatory and residual pore pressure along the depth on several typical lines in the seabed foundations at time $t/T = 46.4$ s. Fig. 12 shows that the oscillatory pore pressure in the upper seabed is generally greater than that in the lower seabed foundations on the same line, and the oscillatory pore pressure in the left part of the seabed is generally greater than that in the right part of seabed. For the residual pore pressure, the distribution is significantly different. The residual pore pressure in the lower seabed is generally much greater than that in the upper seabed. However, the maximum residual pore pressure is not located at the bottom of the seabed foundations. During the initial stage of wave loading, the residual pore pressure in the zone close to the seabed surface builds up to a much greater level than that in other zones. The maximum residual pore pressure occurs in upper seabed. However, the residual pore pressure cannot be excessive due to the limitation of the weight of the soil and structures. After the residual pore pressure reaches the weight of the soil and structures, the seabed becomes liquefied. In addition, the drainage path is relatively short in the upper seabed, thus the residual pore pressure in the liquefied zone in upper seabed decreases gradually due to dissipation. Overall, the depth where the maximum residual pore pressure occurring gradually increases accompanying the downward progressive liquefaction in the process of wave loading. Fig. 12 only show the vertical distribution of the residual pore pressure at time $t/T = 46.4$ s. At this point, the maximum residual pore pressures on lines $x = 140$ m and $x = 170$ m occur around the middle of the seabed foundations. If the wave continues to apply its loading, the depth of the maximum residual pore pressure also continues to increase. It is possible that the maximum residual pore pressure may occur at the bottom of the seabed foundations if the frontier of progressive liquefaction reaches the bottom of the seabed foundations.

(a) Residual pore pressure
(b) Oscillatory pore pressure
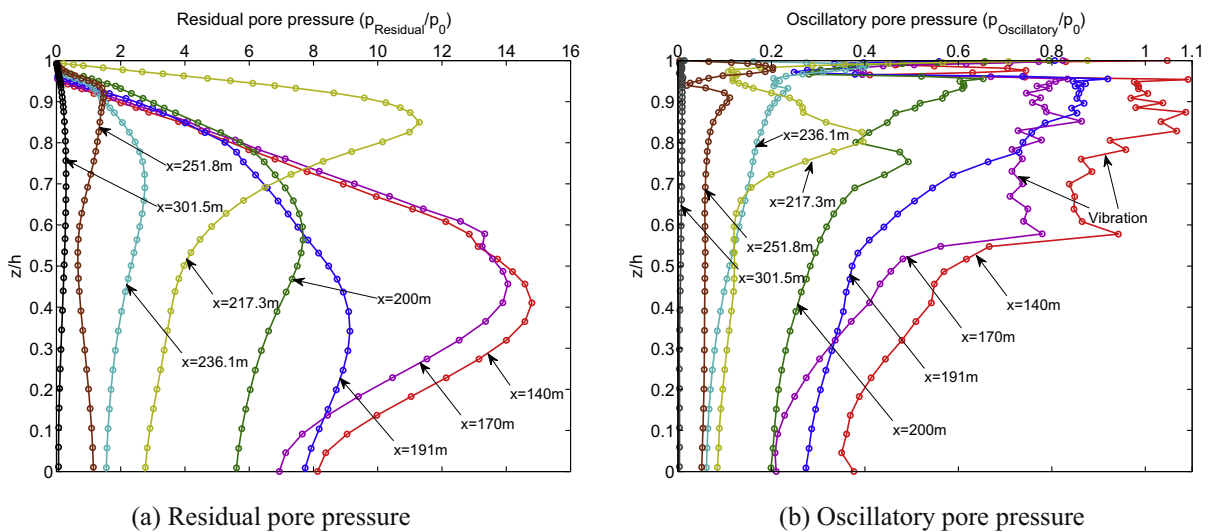
Fig. 12. Distribution of the wave-induced residual and oscillatory pore pressure along the seabed depth at $x = 140$ m, $x = 170$ m, $x = 200$ m, $x = 217$ m, and $x = 236$ m at time $t/T = 46.4$. ($p_0 = H\gamma/(2cosh(\lambda d))$, water depth $d = 15$ m, $H = 3$ m, λ: wave number).

The distribution of the residual pore pressure on the line $x = 217.3$ m, which is the middle line of the composite breakwater, is significantly different from the distribution on the other lines. The maximum residual pore pressure is located in the upper seabed. This type of residual pore pressure distribution is attributable mainly to the wave-induced vibration of the composite breakwater, which makes it much easier for the soil particles in the zone under and close to the composite breakwater to re-arrange their positions. The compaction of the soil in the zone under and close to the composite breakwater is much more intensive than that in other zones.

Similar to the oscillatory pore pressure, the residual pore pressure in the left part of the seabed foundations is much greater than that in the right part of the seabed foundations. This is mainly because the left part of the seabed is affected directly by the wave loading, whereas the right part of seabed foundations generates the excess pore pressure, depending on the pore pressure dissipation and the seepage flow from the left part to the right part of the seabed foundations. The distribution of the oscillatory/residual pore pressure on line $x = 301.5$ m indicates that the effect of pore pressure build up in the left part on the excess pore pressure generation in the right part of the seabed foundations basically disappears in the zone distant from the composite breakwater.

The distribution of the wave-induced oscillatory pore pressure on the lines $x = 140$ m and $x = 170$ m suggest that the distribution of the oscillatory pore pressure in the upper seabed ($z/h = 0.6-1.0$) vibrates along the depth. There is no obvious regulation of the distribution. A comparison of the distributions of the residual pore pressure on the same lines, $x = 140$ m and $x = 170$ m, shows that the distributions of the residual pore pressure in the upper seabed ($z/h = 0.6-1.0$) on the two typical lines are basically sloped straight lines. This indicates that the build up of the residual pore pressure cannot exceed the range constrained by the sloped straight lines. The subsequent analysis shows that after the residual pore pressure in a position reaches the sloped straight lines, the soil becomes liquefied at that position. Therefore, the vibration of the wave-induced oscillatory pore pressure along the seabed depth can be used as an indicator to assess the occurrence of liquefaction and to estimate the wave-induced liquefaction depth in the seabed foundations.

It is also necessary to investigate the distribution of the wave-induced residual and oscillatory pore pressure along the seabed depth at different positions during the wave loading process. In this case, three typical positions, i.e., $x = 140$ m (far from the composite breakwater), $x = 191$ m (close to the composite breakwater), and $x = 200$ m (under the composite breakwater), are selected as representatives. Figs. 13–15 show the distributions of the wave-induced residual and oscillatory pore pressure along the seabed depth at the three typical positions at different times.

Figs. 13–15 show that the wave-induced residual pore pressure in the seabed foundations increases with the time of wave loading. However, the build up of the residual pore pressure is subject to certain constraints because it cannot increase indefinitely. A line (referred to as the liquefaction resistance line in later sections) in the graphs shows the constraint on the residual pore pressure. This line depends on the initial/current stress status, the unit weight of soil, and the internal friction of sandy soil. Its definition is provided in the next section. The residual pore pressure cannot exceed the liquefaction resistance line. When the residual pore pressure at a position reaches the liquefaction resistance line, the wave-induced excess residual pore pressure can overcome the liquefaction resistance of soil. Thus, the soil becomes liquefied in this position at this moment.

Figs. 13 and 14 show that the wave-induced liquefaction is a progressive process in the seabed foundations. The wave-induced liquefaction of the seabed foundations advances downward gradually. On the lines $x = 140$ m and $x = 191$ m, the

(a) Residual pore pressure   (b) Oscillatory pore pressure
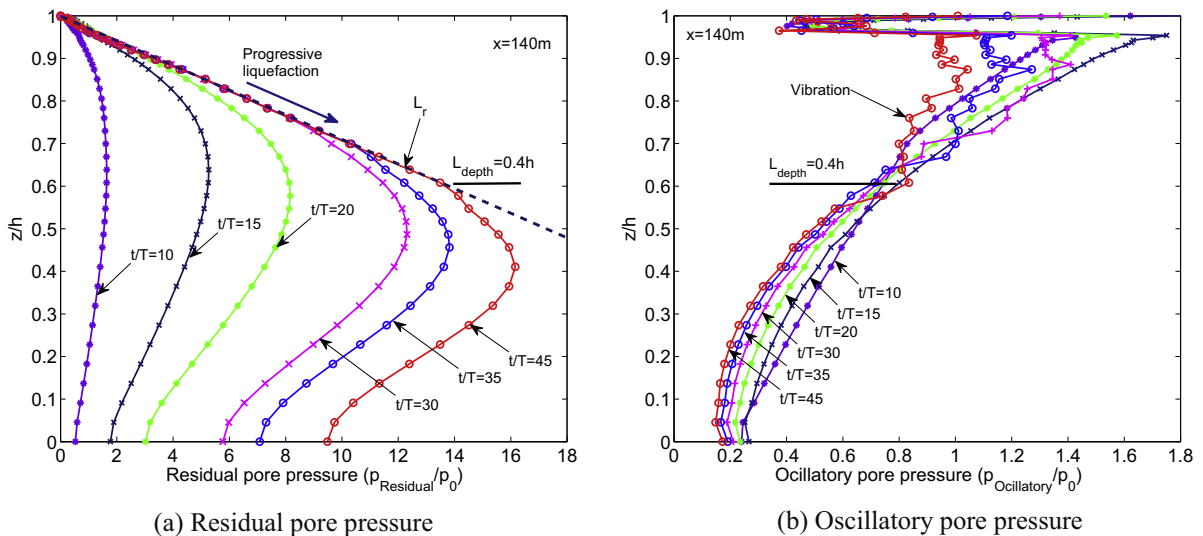
Fig. 13. Distribution of the wave-induced residual and oscillatory pore pressure along the seabed depth at $x = 140$ m (far from the composite breakwater), $\alpha_r = 0.86$.

(a) Residual pore pressure   (b) Oscillatory pore pressure
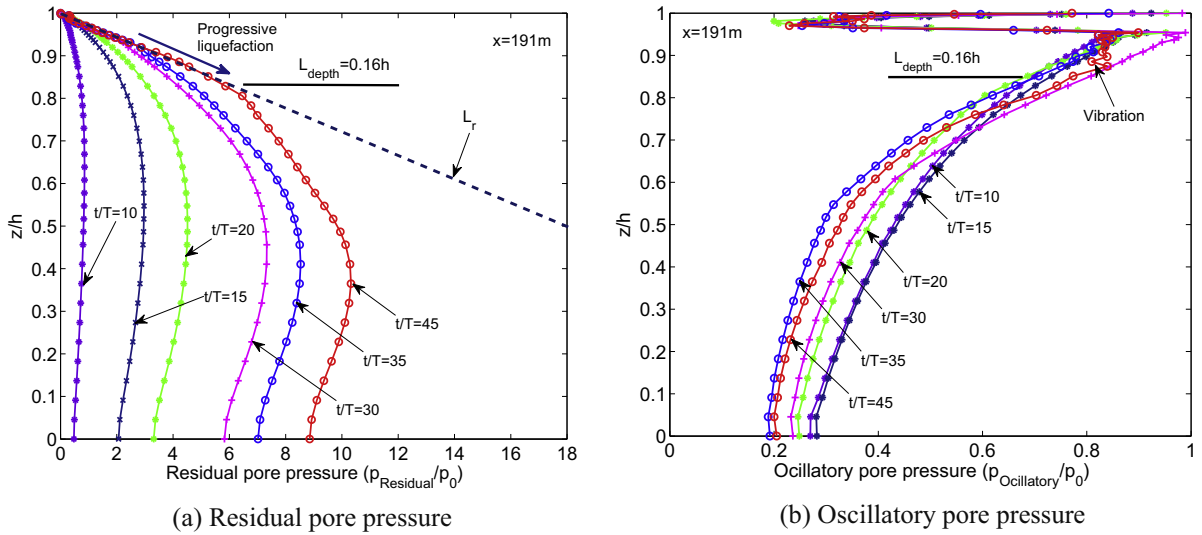
Fig. 14. Distribution of the wave-induced residual and oscillatory pore pressure along the seabed depth at $x = 191$ m (close to the composite breakwater), $\alpha_r = 0.86$.

(a) Residual pore pressure   (b) Oscillatory pore pressure
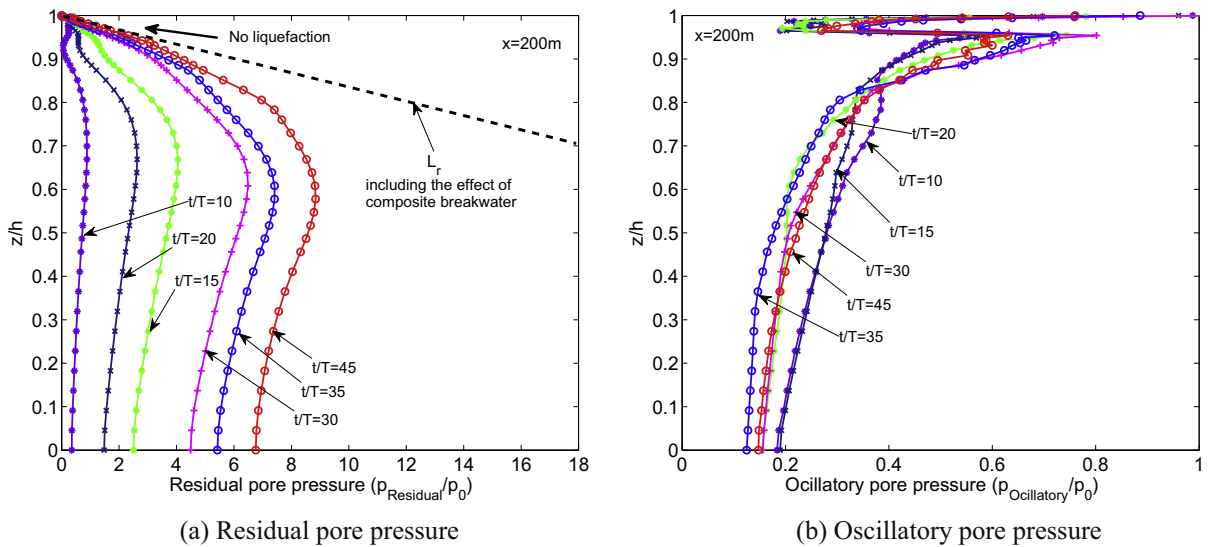
Fig. 15. Distribution of the wave-induced residual and oscillatory pore pressure along the seabed depth at $x = 200$ m (under the composite breakwater).

wave-induced liquefaction depth reaches $0.4h$ and $0.16h$, respectively when $t/T = 45$. The liquefaction depth at $x = 191$ m is much less than that at $x = 140$ m. This may occur because the compression of the composite breakwater means that the initial effective stresses at $x = 191$ m are much greater than those at $x = 140$ m. This results in much greater liquefaction resistance at $x = 191$ m. The distribution of the wave-induced oscillatory pore pressure in Figs. 13 and 14 shows that the distribution of the oscillatory pore pressure also vibrates in the liquefied seabed foundations. This also demonstrates that the vibration of the wave-induced oscillatory pore pressure can be used an indicator of liquefaction.

Fig. 15 shows that there is no liquefaction on the line $x = 200$ m until $t/T = 45$. This is because the gravity of the composite breakwater makes the initial/current effective stresses in the zone under the composite breakwater increase significantly, which leads to a high level of liquefaction resistance on the line $x = 200$ m. There is no liquefaction zone under the composite breakwater, thus the distribution of the wave-induced oscillatory pore pressure does not vibrate accordingly.

Fig. 16 shows the distribution of the effective stresses σ'_x, σ'_z, and the shear stress τ_{xz} in the overall seabed foundations at time $t/T = 46.4$. The following phenomena are observed in Fig. 16. (1) The wave-induced dynamic response, including the effective stresses, shear stress, and pore pressure, are much stronger in the left part of the seabed foundations compared with the right part of the seabed foundations. (2) In the left part of the seabed foundations and in the zone under the composite
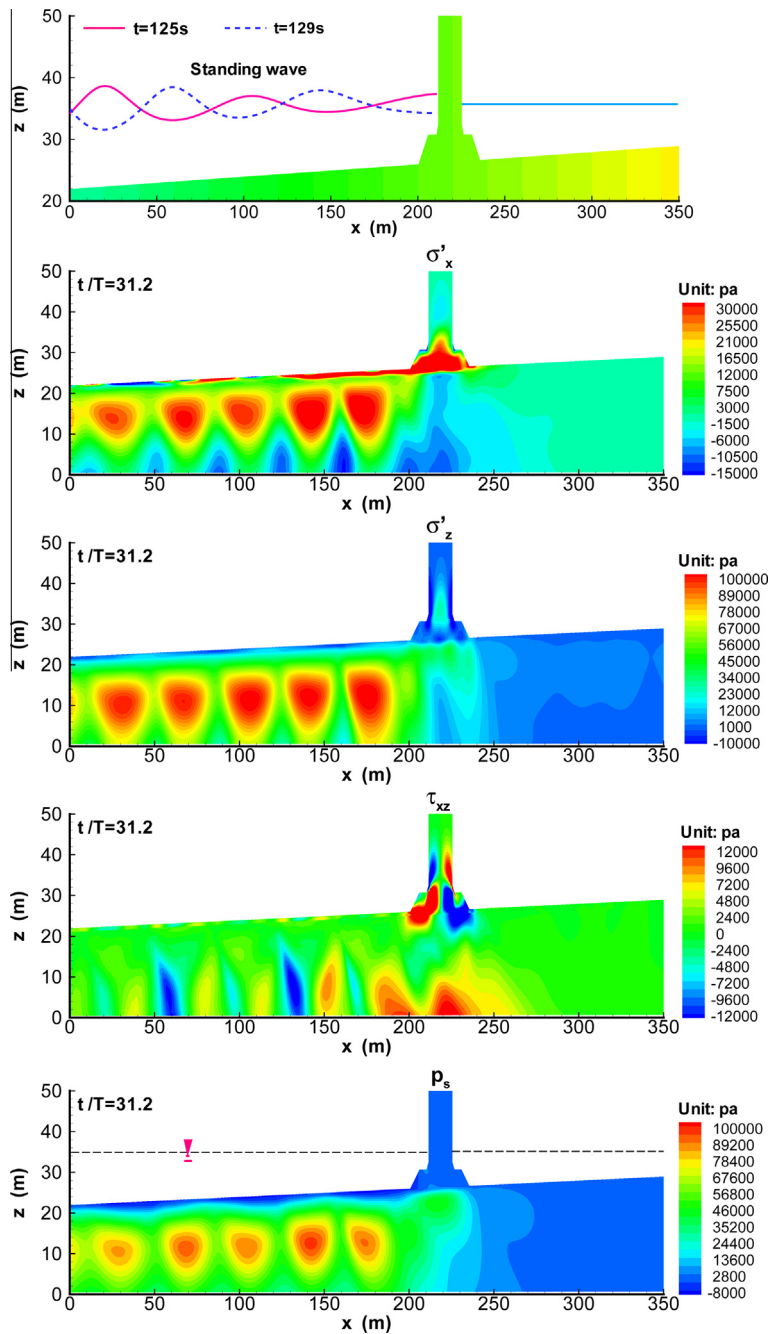
Fig. 16. Distribution of the wave-induced dynamic effective stresses and pore pressure in the seabed foundations at time t/T = 31.2. The wave is almost a standing wave in front of the composite breakwater.

breakwater, there are several shear stress concentration zones in the lower seabed foundations, which were not present before the wave loading. (3) The wave loading makes the pore pressure in the left part of the seabed foundations much greater than that in the right part of the seabed foundations. The high pore pressure dissipates from the left part to the right part of the seabed foundations. Thus, the pore water permeates from the left side to the right side by passing through the region under the composite breakwater, which is driven by the pressure gradient. This effect basically disappears in the zone far from the composite breakwater. (4) In some core regions, the pore pressure is much greater than that in the zones around the core regions. This indicates that the pore pressure buildup is not uniform in the seabed foundations under the standing wave loading. The pore pressure build up is much faster in those core regions under anti-nodes. To the best of our

knowledge, there are no previous reports this phenomenon based on numerical results or experimental tests. This phenomenon was captured for the first time by the numerical model FSSI-CAS 2D.

5.4. Liquefaction potential

As analyzed in the previous section, the pore pressure in the poro-elastoplastic seabed foundation builds up under the wave loading. This reduces the effective contact stresses between soil particles and the seabed foundations soften during this process. Liquefaction occurs when the effective contact stresses between soil particles reach zero. The liquefied seabed behaves like a type of heavy liquid and it loses its bearing capacity. Therefore, the marine structures built on the liquefied seabed foundations will collapse. The liquefaction of the seabed foundations under wave loading is a serious problem that coastal engineers must address during structure design and maintenance. This section investigates the wave-induced residual liquefaction potential of the poro-elastoplastic seabed foundations upon which the composite breakwater is constructed.

Fig. 17 illustrates the stress path of the effective stresses at five typical points in the seabed foundations, which are all close to the seabed surface. Fig. 17 shows that the effective stresses at the five points all decrease gradually during the process of wave loading and they tend to approach the zero stress status (liquefaction). At the positions far from the composite breakwater ($x = 140$ m, $z = 20.8$ m and $x = 170$ m, $z = 22.9$ m), the initial effective stresses are relatively small and the final effective stresses are very close to zero. At the positions under the composite breakwater, especially at the point ($x = 217.3$ m, $z = 23.8$ m), the initial effective stresses are relatively large due to the compression of the composite breakwater and the final effective stresses are far from the zero stress status. As mentioned in the previous section, this mainly because the compression of the composite breakwater can effectively prevent the effective contact stresses in the region under the composite breakwater from becoming zero. In Fig. 17, the stress path for point ($x = 217.3$ m, $z = 23.8$ m) is also plotted based on elastic seabed foundations. The effective stresses cannot decrease because no residual pore pressure is generated in the elastic seabed under wave loading. Thus, the stress path can only form circles.

Okusa [61] proposed 1D liquefaction criteria based on the initial and wave-induced vertical effective stress σ'_{z0} and σ'_{zd}:

$$\sigma'_{zd} \geqslant -\sigma'_{z0} \tag{23}$$

where σ'_{z0} is considered to be the prevention of liquefaction and σ'_{zd} is the wave-induced dynamic vertical effective stress, which is the driving force of liquefaction. However, previous studies have not considered the effects of initial horizontal effective stresses σ'_{x0} and σ'_{y0} on preventing liquefaction. Tsai [12] further extended the above 1D liquefaction criteria to 3D conditions:

$$\frac{1}{3}(\sigma'_{x0} + \sigma'_{y0} + \sigma'_{z0}) + \frac{1}{3}(\sigma'_{xd} + \sigma'_{yd} + \sigma'_{zd}) \geqslant 0 \tag{24}$$

where σ'_{xd} and σ'_{yd} are the wave-induced dynamic horizontal effective stress. These liquefaction criteria only employ the average. Thus, there is no clear physical meaning of how the horizontal effective stresses σ'_x and σ'_y affect the liquefaction potential of soil. Recently, Ye [62] proposed further 3D liquefaction criteria to consider the effects of cohesion and the internal friction angle of the soil:

$$\sigma'_z + 2(c - \sigma'_x \tan \phi)u(-\sigma'_x) + 2(c - \sigma'_y \tan \phi)u(-\sigma'_y) \geqslant 0 \tag{25}$$

where $u(x)$ is the unit step function
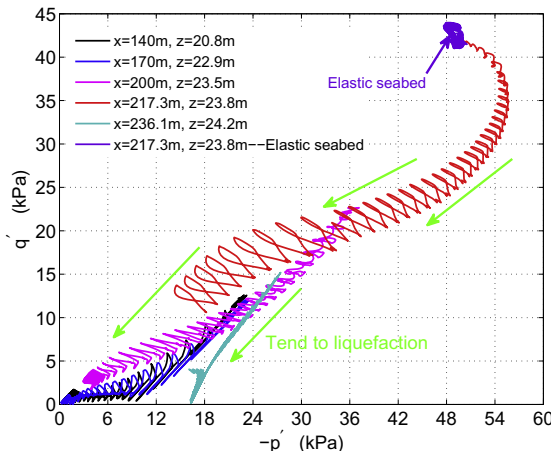
Fig. 17. The stress path of the effective stresses at five typical points located close to the seabed surface under wave loading.

$$u(x) = \begin{cases} 1 & x > 0 \\ 0 & x \leqslant 0 \end{cases} \tag{26}$$

where the c and ϕ are the cohesion and internal friction of soil, respectively. For sandy soil, the cohesion c is normally 0. Ye [62] claims that the 3D liquefaction criteria proposed by Tsai [12] are a special form of the liquefaction criteria that consider the cohesion of the friction angle when $c = 0$ and $\phi = 26.6°$. Considering that $\sigma'_z = \sigma'_{z0} + \sigma'_{zd}$, the residual liquefaction potential is defined in the following form based on the liquefaction criterion in the present study (25).

$$L_{potential} = \frac{\sigma'_{zd}}{-\sigma'_{z0} - 2(c + (-\sigma'_x)\tan\phi)u(-\sigma'_x) - 2(c + (-\sigma'_y)\tan\phi)u(-\sigma'_y)} \tag{27}$$

In theory, when the $L_{potential}$ is greater than or equal to 1.0 at a certain position, the soil is liquefied at that position. Clearly, the liquefaction potential of the soil would be overestimated if the cohesion and internal friction of the soil are not taken into consideration in the analysis. However, the $L_{potential}$ does not exceed 1.0 in numerical computations or in laboratory tests [63,64] because sandy soil is a non-cohesive granular material and it cannot bear any tensile stress. There is no yield surface or plastic potential surface in the tension stress space. The PZIII soil model cannot describe the soil behaviors under tensile stress [49]. Therefore, the soil cannot reach a completely liquefied state in numerical computations, i.e., the ratio between the excess residual pore pressure and the liquefaction resistance of the soil cannot reach 1.0. Furthermore, Ishihara [63] suggested that the pore water pressure ratio did not develop fully in silty sands or sandy silts containing some amount of fines, but instead they stopped building up when they reached a value equal to about 0.9 to 0.95 of the liquefaction resistance. If liquefaction is strictly defined as the occurrence of the full pore pressure ratio of 1.0, then these soils would never "liquefy" although they may behave as liquefiable materials. Some laboratory soil tests [64,65] performed at U.C. Berkeley also showed that liquefaction could still occur when the residual excess pore pressure did not reach the downward initial vertical effective stress. This means that liquefaction is highly possible even if $L_{potential} \leqslant 1.0$. Based on the conclusions of previous tests, we assume that the soil will liquefy if $L_{potential} \geqslant \alpha_r$

$$L_{potential} = \frac{\sigma'_{zd}}{-\sigma'_{z0} - 2(c + (-\sigma'_x)\tan\phi)u(-\sigma'_x) - 2(c + (-\sigma'_y)\tan\phi)u(-\sigma'_y)} \geqslant \alpha_r \tag{28}$$

where α_r is a coefficient that depends on the soil characteristics, which generally has a range of 0.78–0.99 [64]. Therefore, the liquefaction resistance of soil can be defined as follows.

$$L_r = \alpha_r(-\sigma'_{z0} - 2(c + (-\sigma'_x)\tan\phi)u(-\sigma'_x) - 2(c + (-\sigma'_y)u(-\sigma'_y)\tan\phi)) \tag{29}$$

Using the definition of the liquefaction potential given in Eq. (27), we analyze the liquefaction potential of the poro-elastoplastic seabed foundations under the wave loading. Fig. 18 shows the time curves of the liquefaction potential at three typical positions: A ($x = 140$ m, $z = 22.3$ m), B ($x = 170$ m, $z = 22.9$ m), and C ($x = 200$ m, $z = 23.5$ m), during the wave loading process ($c = 0, \phi = 35°$). Fig. 18 indicates that the liquefaction potential in the seabed foundations under the wave loading increases gradually to a peak value before decreasing to a constant value. The existence of a peak liquefaction potential may occur because pore pressure build up and pore pressure dissipation exist simultaneously in the seabed foundations. The three points selected are all close to the seabed surface, thus the effect of pore pressure dissipation cannot be ignored. If the rate of pore pressure dissipation is greater than the rate of pore pressure build up, the pore pressure will decrease in the zone close to the seabed surface and the liquefaction potential decreases. At position C ($x = 200$ m, $z = 23.5$ m), which is under the left foot of the rubble mound, the initial effective stresses are relatively large because of the compression of the
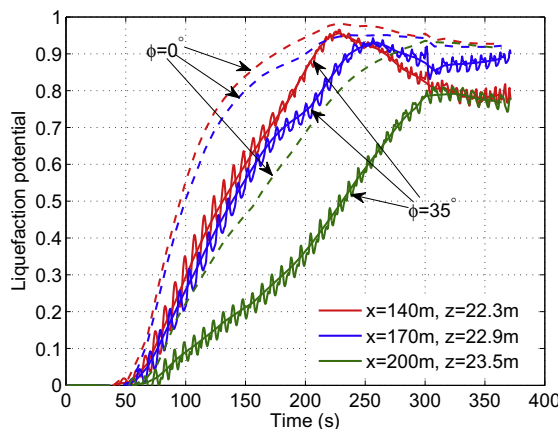
Fig. 18. Historic curve of the liquefaction potential at points A ($x = 140$ m, $y = 22.5$ m), B ($x = 170$ m, $y = 22.9$ m), and C ($x = 200$ m, $y = 23.5$ m).

composite breakwater and the liquefaction resistance is very high at position C. Thus, the liquefaction potential is relatively low compared with the other two positions. Due to the compression of the composite breakwater, the growth rate of the liquefaction potential at position C is also significantly lower than that at the other two positions.

The time curves for the liquefaction potential at the three points are also plotted in Fig. 18, where the internal friction angle $\phi = 0°$. Fig. 18 shows that the residual liquefaction potential in the seabed foundations is overestimated significantly when the internal friction angle of the soil is not considered. Thus, it is recommended that the friction angle of the sandy soil is considered when evaluating the wave-induced liquefaction potential in the seabed foundations.

Fig. 19 shows the distribution of the liquefaction potential along the depth on several typical lines: $x = 140$ m, $x = 170$ m, $x = 200$ m, and $x = 250$ m. In Fig. 19, the liquefaction potential in the seabed foundations increases with the time of wave loading. This is mainly because the residual pore pressure becomes increasingly greater during the wave loading process. The lines $x = 140$ m and $x = 170$ m are far from the composite breakwater, thus the effect of the composite breakwater's compression on the effective stresses on the two lines is insignificant. The liquefaction potential on lines $x = 140$ m and $x = 170$ m is also generally greater than that on the line $x = 200$ m at the same time. The right part of the seabed foundations is not affected directly by the wave loading, thus the liquefaction potential in the right part of the seabed foundations appears to be small compared with that in the left part of the seabed foundations. It is interesting that the liquefaction potential in the zone near to the seabed surface decreases sharply during the later stage of wave loading. This phenomenon can also be explained by the fact that the pore pressure build up and dissipation exist simultaneously in the seabed foundations under the wave loading. In the zone near to the seabed surface, the drainage distance is short and the drainage is relatively unobstructed. The residual pore pressure accumulate less readily due to the low plastic volumetric deformation during the late stage of wave loading, while the pore pressure dissipates freely from the zone near to the seabed surface.

Based on the distribution of the liquefaction potential on the lines $x = 140$ m and $x = 170$ m at time $t/T = 46.25$, it can be seen that the upper seabed foundations are liquefied when the liquefaction potential $L_{potential} \geqslant 0.86$. Therefore, the coefficient α_r is 0.86 based on this result. Indeed, α_r also can be determined to be 0.86 based on the slope of the liquefaction resistance line in Figs. 13 and 14, which indicates that $\alpha_r = 0.86$ for Nevada dense sand.

The liquefaction potential distributions on the lines $x = 140$ m, $x = 170$ m, $x = 200$ m, and $x = 250$ m are also plotted in Fig. 19, where the internal friction angle $\phi = 0°$. This also demonstrates that the residual liquefaction potential in the seabed foundations is significantly overestimated if the internal friction angle of the soil is not considered.

Figs. 13 and 14 show that the wave-induced liquefaction in the seabed foundation proceeds from the upper seabed to the lower seabed, i.e., the liquefaction front advances downward gradually. This phenomenon was also observed in a centrifuge test described by Sassa and Sekiguchi [30]. Fig. 20 illustrates the progression of wave-induced liquefaction in the seabed foundations based on the lines $x = 140$ m, $x = 170$ m, and $x = 191$ m, which shows that the wave-induced liquefaction depth in the seabed foundations increases gradually with time. On the lines $x = 140$ m and $x = 170$ m, the liquefaction depth reaches
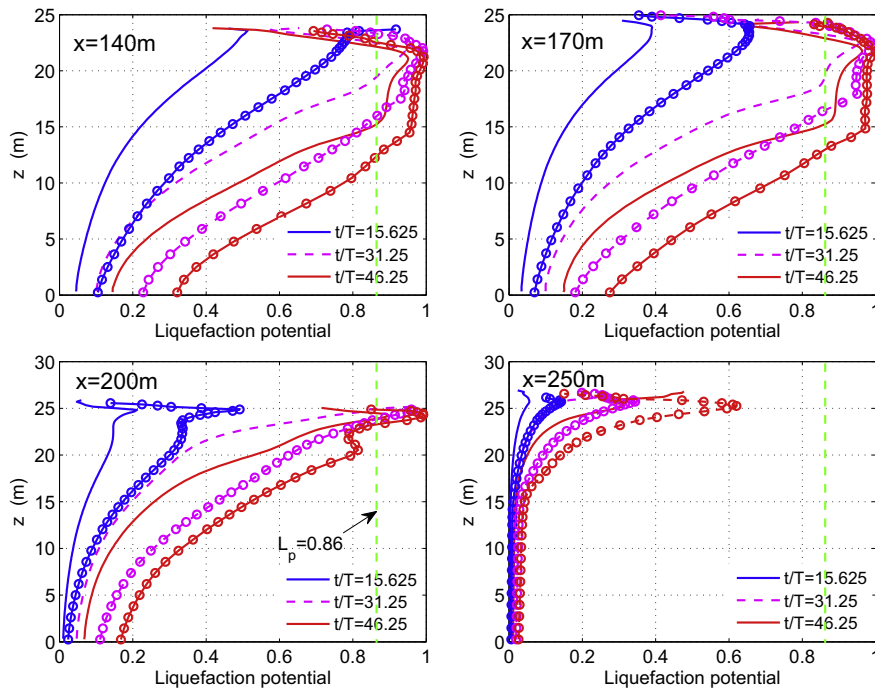
Fig. 19. Distribution of the wave-induced liquefaction potential in the seabed foundations on the lines $x = 140$ m, $x = 170$ m, $x = 200$ m and $x = 250$ m at different times. Note that the lines without circles are the results when $\phi = 35°$, whereas the lines with circles are the results when $\phi = 0°$.
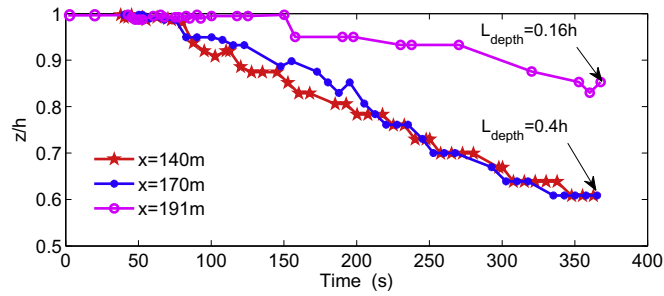
Fig. 20. Progressive liquefaction process in the seabed foundations along $x = 140$ m, $x = 170$ m, and $x = 200$ m.
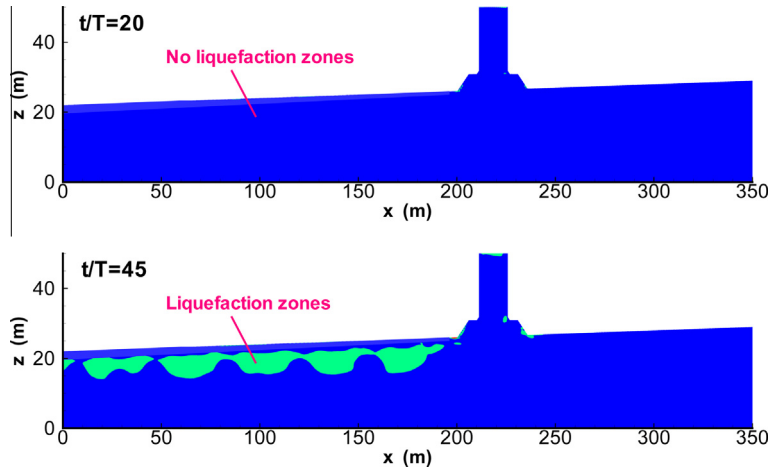
Fig. 21. Predicted liquefaction zone in the seabed foundations at two typical times: $t/T = 20$ and $t/T = 45$ ($L_{potential} \geqslant 0.86$).

0.4 h at time $t = 370$ s, but it is only 0.16 h on the line $x = 191$ m. This indicates that the compression of the composite breakwater can prevent liquefaction in the region nearby.

Fig. 21 shows the predicted wave-induced liquefaction zone in the seabed foundations at two typical times: $t/T = 20$ and $t/T = 45$. During the early stage of wave loading, the residual excess pore pressure is insufficient to overcome the weight of the soil and the composite breakwater, thus there is no liquefaction zone. During the later stage of wave loading, the residual excess pore pressure builds up to values that approach the liquefaction resistance level. When the liquefaction potential $L_{potential} \geqslant 0.86$ in a zone, the zone becomes liquefied. In Fig. 21, liquefaction occurs mainly in the zones under the anti-nodes of the standing wave. Under the nodes, the liquefaction zones are apparently small. This phenomenon occurs because the seabed foundations under the anti-nodes of the standing wave are loaded intensively by the wave, whereas the seabed foundations under the nodes are not affected by the wave because the nodes retain their positions at the static water level. It can also be seen that there is no liquefaction zone in the areas under the composite breakwater and to the right of the seabed foundations. An interesting phenomenon shown in Fig. 21 is that the sandy soil in the zone close to the seabed surface does not liquefy during the later stage of the wave loading process. This is because the dissipation of the pore pressure is faster than the build up of the pore pressure in this zone. The residual excess pore pressure is insufficient to overcome the weight of the soil in the zone near to the seabed surface in the later stage of the wave loading process.

5.5. Parametric study

In the analysis described above, the seabed foundations comprised Nevada dense sand with standard parameters ($k = 1.0 \times 10^{-5}$ m/s, $S_r = 98\%$, $H = 3.0$ m, $T = 8.0$ s, $d = 15$ m). Understanding how the parameters affect the pore pressure build up and the liquefaction potential in the seabed foundations under wave loading is problematic. In this section, a parametric study is conducted to investigate the effects of the soil properties and wave characteristics on the pore pressure build up and the liquefaction potential in the seabed foundations. In this case, only position A ($x = 170$ m, $z = 22.9$ m) is used as a representative point to demonstrate the effects of the parameters.

Fig. 22 Illustrates the effects of the wave height (H) and wave period (T) on the liquefaction potential at position A ($x = 170$ m, $z = 22.9$ m) in the seabed foundations under wave loading. It can be seen that the wave height and wave period
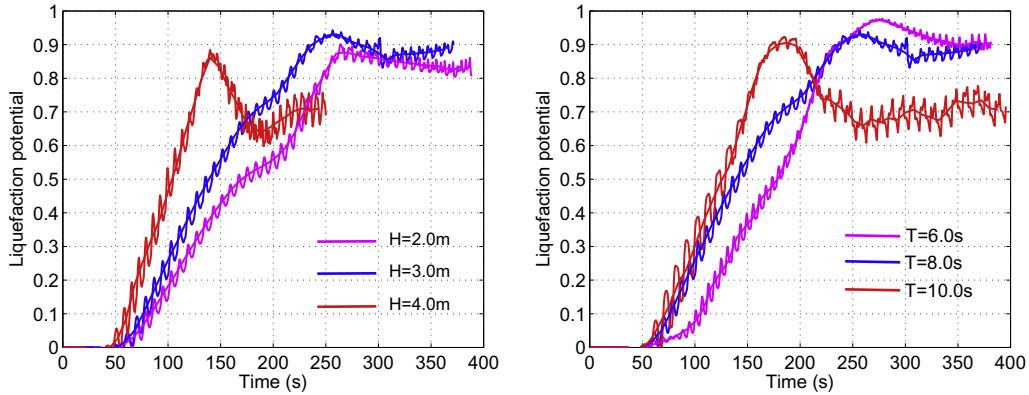
Fig. 22. Effects of the wave height and period on the liquefaction potential at ($x = 170$ m, $z = 22.9$ m) in the seabed foundations under wave loading.

have significant effects on the liquefaction potential in the seabed foundations. The pore pressure builds up faster when the wave is higher, or the wave period is longer, and the growth rate of the liquefaction potential is greater. This phenomenon occurs because a higher wave and/or a wave with a longer period carries more energy, thus the wave loading that acts on the seabed is greater. The time required for the liquefaction potential to vary from zero to its peak value is relatively shorter. During the later stage of wave loading, the liquefaction potential in the seabed foundations under wave loading with a greater height and/or longer period is smaller than that under a wave loading with a lower height and/or shorter period. This phenomenon occurs because the plastic volumetric deformation of the soil is larger under a wave loading with a greater height and/or longer period during the early stage, thereby making the pore pressure build up very rapidly, whereas the plastic volumetric deformation of the soil is basically zero under the same wave loading during the later stage. The dissipation of the residual pore pressure also occurs, which makes the residual excess pore pressure in the seabed foundations decrease. This leads directly to a reduction of the liquefaction potential during the later stage of wave loading.

Fig. 23 shows the effects of the permeability and saturation of the seabed soil on the liquefaction potential at position A ($x = 170$ m, $z = 22.9$ m). Based on Fig. 23, we can conclude that the permeability of the seabed soil is the most important parameter that affects the liquefaction of soil. Thus, it is difficult for the pore pressure to build up in a soil with high permeability. Therefore, a soil with high permeability, such as coarse sand, is unlikely to liquefy under the wave loading because the residual pore pressure is readily dissipated. The saturation of the soil also significantly affects the liquefaction potential of the seabed foundations. Compared with a saturated soil, an unsaturated soil is more likely to liquefy under the wave loading. Thus, the growth rate of the liquefaction potential is related negatively to the saturation of the soil.

In addition, a parametric study investigated the effects of the wave characteristics and soil properties on the progressive liquefaction of the seabed foundations. Fig. 24 shows the effect of the wave height and wave period on the progressive liquefaction process on the line $x = 140$ m. In Fig. 24(a), the effects of the wave characteristics on the progressive liquefaction appear to be fairly complex. It is not difficult to understand that the liquefaction depth is greatest, i.e., 0.58 h at time $t/T = 38$, when the wave height is 4 m. However, it is somewhat surprising that the liquefaction depth is 0.48 h at time $t/T = 45$ when $H = 2.0$ m, which is deeper than that when $H = 3.0$ m. In Fig. 24(b), the liquefaction depth is the same when the wave period is 6 s and 8 s, while the liquefaction depth is only 0.23 h when the wave period is 10 s at the time $t/T = 45$. The liquefaction depth under the wave loading with a longer period is less than that when the wave period is shorter. This phenomenon
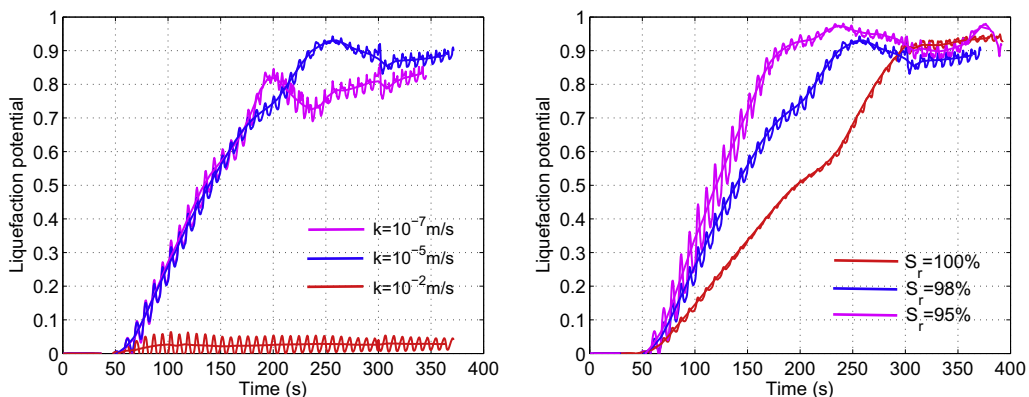
Fig. 23. Effects of seabed soil permeability and saturation on the liquefaction potential at ($x = 170$ m, $z = 22.9$ m) in the seabed foundations under wave loading.
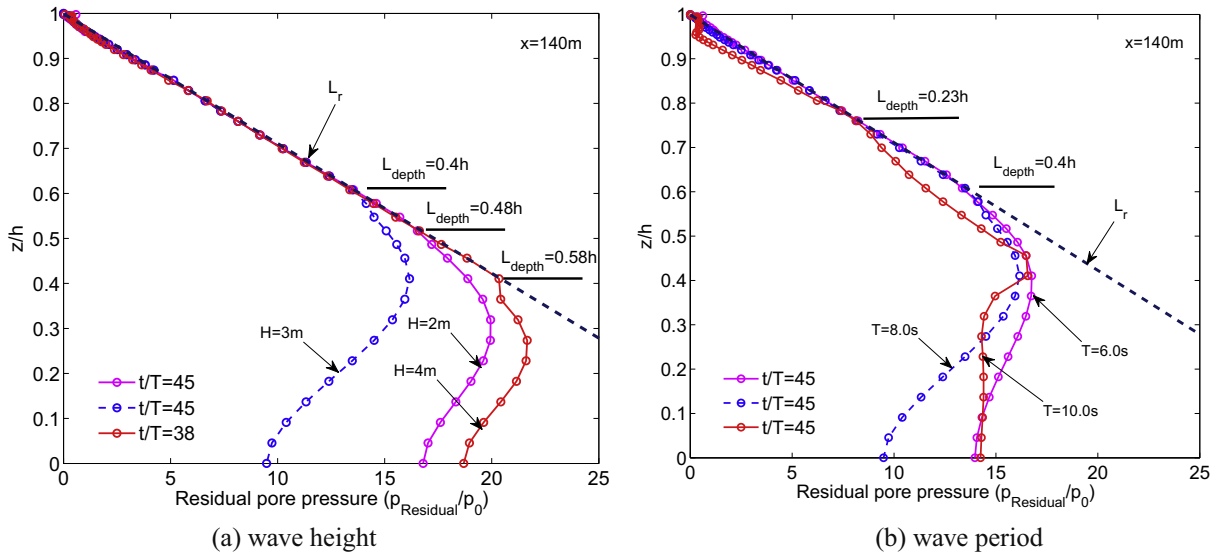
Fig. 24. Effects of the wave height and period on the progressive liquefaction process at the typical position $x = 140$ m ($\alpha_r = 0.86$).
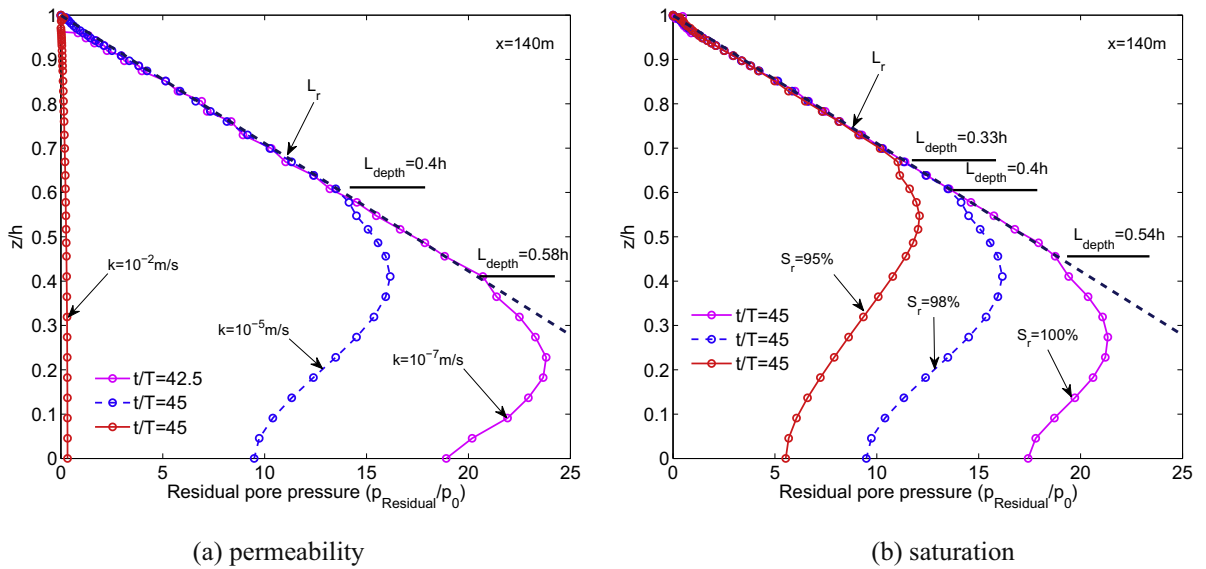
Fig. 25. Effects of seabed soil permeability and saturation on the progressive liquefaction process at the typical position $x = 140$ m ($\alpha_r = 0.86$).

occurs because the residual pore pressure cannot build up continuously under wave loading and the dissipation of the pore pressure reduces the residual pore pressure in the later stage of wave loading. Under the wave with a longer loading period, the liquefaction depth reaches its maximum value (> 0.4 h) during the middle stage of wave loading, after which the lique-faction front moves upward gradually in the later stage of wave loading because of the reduced residual pore pressure. This process is known as "densification."

Fig. 25 illustrates the effects of the permeability and saturation of the soil on the progressive liquefaction process on the line $x = 140$ m. In Fig. 25(a) and (b), the depth of the progressive liquefaction in the seabed foundations is related negatively to the soil permeability and related positively to the soil saturation.

6. Conclusions

This study investigated the wave-induced dynamic response of a composite breakwater built on poro-elastoplastic sea-bed foundations using the integrated model FSSI-CAS 2D, where the dynamic Biot's equation "$u - p$" approximation governs the dynamic behaviors of the porous medium in the soil model and the VARANS equation governs the flow of fluid inside and outside the porous medium in the wave model. The PZIII model proposed by Pastor et al. [45] was used to model the

behaviors of the poro-elastoplastic seabed foundations in computations. The following conclusions are suggested based on the results presented in this study.

(1) It is important to determine the initial consolidation state of the seabed foundations under the hydrostatic pressure and composite breakwater loading. This consolidation state should be used as the initial boundary conditions for the following dynamic analysis. The initial resistance to soil liquefaction should also be determined.

(2) Under wave loading, the pore pressure builds up in the poro-elastoplastic seabed foundations because of soil compaction under cyclic wave loading, thereby reducing the effective contact stresses between the soil particles, which softens the seabed foundations. Thus, excessive settlement and tilting affect the composite breakwater built on the seabed foundations. This is a dangerous factor for the stability of the composite breakwater. Therefore, Quaternary newly deposited loose seabed foundations are not suitable for uses as the foundations of marine structures in general. If this situation cannot be avoided, the performance of marine structures should be evaluated based on the hydrodynamic conditions selected in the design stage.

(3) In the zone far from the composite breakwater, the effective stress status is not affected by the composite breakwater and the pore pressure can build up to an adequate level. During the later stage of wave loading, the effective stresses σ'_x, σ'_z, and the shear stress τ_{xz} approach the zero stress status. The seabed foundations liquefy within a certain depth. However, in the zone near to marine structures, the initial effective stresses are relatively large due to the compression of the composite breakwater and the effective contact stresses σ'_x, σ'_z, and shear stress τ_{xz} are unlikely to become zero during the wave loading process. Therefore, in the zone near to marine structures, the seabed foundations are less likely to liquefy under wave loading.

(4) The pore pressure in the seabed foundations includes oscillatory and residual components. The oscillatory pore pressure in the upper seabed is generally greater than that in the lower seabed. By contrast, the residual pore pressure in the lower seabed is greater than that in the upper seabed. The right part of the seabed is not affected directly by the wave loading, thus the oscillatory/residual pore pressure in the right part of the seabed is much less than that in the left part of the seabed. The generation of oscillatory and residual pore pressure in the right part of the seabed indicates that the pore water permeates from the left part to the right part of the seabed, which is driven by the pressure gradient.

(5) The pore pressure builds up under the wave loading in the seabed foundations, but it is subjected to some constraints because it cannot exceed the liquefaction resistance line. After the residual pore pressure reaches the liquefaction resistance line at a certain position, the seabed soil becomes liquefied in that position. The liquefaction process moves downward. The distribution of the oscillatory pore pressure fluctuates in the liquefied seabed foundations. This fluctuation can be used as an indicator to assess the occurrence of liquefaction and to estimate the liquefaction depth during analyses.

(6) In poro-elastoplastic seabed foundations, the build up of wave-induced pore pressure reduces the effective stresses. The stress path moves toward the zero stress status (complete liquefaction). In the zone far from the composite breakwater, the stress path finally arrives at the points that are very close to the zero stress status. By contrast, in the zone near to the composite breakwater, the stress path can only arrive at the points far from the zero stress status. Thus, the liquefaction potential in the zone far from the composite breakwater is greater than that in the zone near to the composite breakwater.

(7) The proposed definitions of the liquefaction potential ($L_{potential}$) and liquefaction resistance L_r consider the effects of cohesion and the internal friction angle of the soil. The analysis showed that the liquefaction potential in the seabed foundation increases with time under wave loading. The effect of the friction angle of the soil on the liquefaction potential is significant. The liquefaction potential $L_{potential}$ never reaches 1.0 exactly in laboratory tests or in numerical computations. Nevada dense sand is liquefied when $L_{potential} \geqslant 0.86$.

(8) The parametric study indicates that a higher wave and/or a wave with a longer period increased the growth rate of the liquefaction potential during the early stage of wave loading. The existence of densification induced by pore pressure dissipation after liquefaction in the sandy seabed under long term wave loading makes it difficult to generalize the trend in the liquefaction potential of the seabed during the later stage of wave loading. For example, the liquefaction potential of the seabed with a higher wave and/or a wave with a longer period is less than that with a smaller wave and/or a wave with a shorter period during the later stage of wave loading. Thus, it is highly dependent on time. The soil permeability is the most important parameter that affects the pore pressure build up and liquefaction potential. The soil saturation also has a significant effect on the liquefaction potential. A saturated soil with high permeability is most unlikely to liquefy under wave loading.

References

[1] H.E. Harlow, Large rubble-mound breakwater failures, J. Waterw. Port Coastal Ocean Eng. ASCE 106 (2) (1980) 275–278.
[2] K. Zen, Y. Umehara, W.D.L. Finn, A case study of the wave-induced liquefaction of sand layers under damaged breakwater, in: Proceeding 3rd Canadian Conference on Marine Geotechnical Engineering, Canada, pp. 505–520, 1985.
[3] R. Silvester, J.R.C. Hsu, Sines revisited, J. Waterw. Port Coastal Ocean Eng. ASCE 115 (3) (1989) 327–344.

[4] H. Lundgren, J.H.C. Lindhardt, C.J. Romold, Stability of breakwaters on porous foundation, in: Proceeding of 12th International Conference on Soil Mechanics and Foundation Engineering, vol. 1, pp. 451–454, 1989.
[5] T. Sorenson, Breakwater failure brings lessons (ltr), Civil Eng. – ASCE 62 (9) (1992) 37–38.
[6] H. Oumeraci, Review and analysis of vertical breakwater failures lessons learned special issue on vertical breakwaters, Coastal Eng. 22 (1994) 3–29.
[7] Leopoldo Franco, Vertical breakwaters: the italian experience, Coastal Eng. 22 (1-2) (1994) 31–55.
[8] F.G. Zhang, Z.J. Ge, A study on some causes of rubble mound breakwater failure, China Ocean Eng. 10 (4) (1996) 473–481.
[9] P.M. Guillen, Large breakwaters in deep water in northern spain, Proc. Inst. Civ. Eng. Marit. Eng. 161 (MA4) (2008) 175–186.
[10] T. Yamamoto, H.L. Koning, H. Sellmeijer, E.V. Hijum, On the response of a poro-elastic bed to water waves, J. Fluid Mech. 87 (1) (1978) 193–206.
[11] J.R.C. Hsu, D.S. Jeng, Wave-induced soil response in an unsaturated anisotropic seabed of finite thickness, Int. J. Numer. Anal. Methods Geomech. 18 (11) (1994) 785–807.
[12] C.P. Tsai, Wave-induced liquefaction potential in a porous seabed in front of a breakwater, Ocean Eng. 22 (1) (1995) 1–18.
[13] M.B.C. Ulker, M.S. Rahman, D.S. Jeng, Wave-induced response of seabed: various formulation and their applicability, Appl. Ocean Res. 31 (2009) 12–24.
[14] H. Mase, T. Sakai, M. Sakamoto, Wave-induced porewater pressure and effective stresses around breakwater, Ocean Eng. 21 (4) (1994) 361–379.
[15] M.B.C. Ulker, M.S. Rahman, M.N. Guddati, Wave-induced dynamic response and instability of seabed around caisson breakwater, Ocean Eng. 37 (17-18) (2010) 1522–1545.
[16] M.B.C. Ulker, M.S. Rahman, M.N. Guddati, Breaking wave-induced response and instability of seabed around caisson breakwater, Int. J. Numer. Anal. Methods Geomech. 36 (3) (2012) 362–390.
[17] N. Mizutani, A. Mostarfa, K. Iwata, Nonlinear regular wave, submerged breakwater and seabed dynamic interaction, Coastal Eng. 33 (1998) 177–202.
[18] A. Mostafa, N. Mizutani, K. Iwata, Nonlinear wave, composite breakwater, and seabed dynamic interaction, J. Waterw. Port Coastal Ocean Eng. ASCE 25 (2) (1999) 88–97.
[19] H. Nago, S. Maeno, T. Matsumoto, Y. Hachiman, Liquefaction and densification of loosely deposited sand bed under water pressure variation, in: Proceeding of the 3rd international offshore and Polar Engineering Conference, Singapore, pp. 578–584, 1993.
[20] K. Zen, H. Yamazaki, Oscillatory pore pressure and liquefaction in seabed induced by ocean waves, Soils Found. 30 (4) (1990) 147–161.
[21] B. Choudhury, G.R. Dasari, T. Nogami, Laboratory study of liquefaction due to wave-seabed interaction, J. Geotech. Geoenviron. Eng. ASCE 132 (7) (2006) 842–851.
[22] M. Mory, H. Michallet, D. Bonjean, I. Piedra-Cueva, J.M. Barnoud, P. Foray, S. Abadie, P. Breul, A field study of momentary liquefaction caused by waves around a coastal structure, J. Waterw. Port Coastal Ocean Eng. ASCE 133 (1) (2007) 28–38.
[23] B.M. Sumer, J. Fredsoe, S. Christensen, M.T. Lind, Sinking/floatation of pipelines and other objects in liquefied soil under waves, Coastal Eng. 38 (2) (1999) 53–90.
[24] B.M. Sumer, C. Truelsen, J. Fredsoe, Liquefaction around pipelines under waves, J. Waterw. Port Coastal Ocean Eng. ASCE 132 (4) (2006) 266–275.
[25] M.B. Sumer, F.H. Dixen, J. Fredsoe, Cover stones on liquefiable soil bed under waves, Coastal Eng. 57 (9) (2010) 864–873.
[26] T.C. Teh, A.C. Palmer, J.S. Damgaard, Experimental study of marine pipelines on unstable and liquefied seabed, Coastal Eng. 50 (1-2) (2003) 1–17.
[27] S.-Y. Tzang, S.-H. Ou, T.W. Hsu, Laboratory flume studies on monochromatic wave-fine sandy bed interactions part 2. Sediment suspensions, Coastal Eng. 56 (3) (2009) 230–243.
[28] S.-Y. Tzang, Y.L. Chen, S.-H. Ou, Experimental investigations on developments of velocity field near above a sandy bed during regular wave-induced fluidized responses, Ocean Eng. 38 (7) (2011) 868–877.
[29] S. Sassa, T. Takayama, M. Mizutani, D. Tsujio, Field observations of the build-up and dissipation of residual porewater pressures in seabed sands under the passage of stormwaves, J. Coastal Res. 39 (2006) 410–414.
[30] S. Sassa, H. Sekiguchi, Wave-induced liquefaction of beds of sand in a centrifuge, Géotechnique 49 (5) (1999) 621–638.
[31] J.H. Ye, Numerical analysis of wave-seabed-breakwater interactions (PhD thesis), University of Dundee, Dundee, UK, May 2012.
[32] J.H. Ye D.-S. Jeng, Response of porous seabed to nature loadings-waves and currents, J. Eng. Mech. ASCE 138 (6) (2012) 601–613.
[33] D.-S. Jeng, J.H. Ye, J.-S. Zhang, P.L.-F. Liu, An integrated model for the wave-induced seabed response around marine structures: model, verifications and applications, Coastal Eng. 72 (1) (2013) 1–19.
[34] J.H. Ye, D.-S. Jeng, R. Wang, C.Q. Zhu, Numerical study of the stability of breakwater built on sloped porous seabed under tsunami loading, Appl. Math. Model. 37 (2013) 9575–9590.
[35] J.H. Ye, D.-S. Jeng, P.L.-F. Liu, A.H.C. Chan, R. Wang, C.Q. Zhu, Breaking wave-induced response of composite breakwater and liquefaction of seabed foundation, Coastal Eng, 73 (2014). http://dx.doi.org/10.1016/j.coastaleng.2013.08.003, in press.
[36] M.S. Rahman, W.Y. Jaber, Simplified drained analysis for wave-induced liquefaction in ocean floor sands, Soils Found. 26 (3) (1986) 57–68.
[37] L. Cheng, B.M. Sumer, J. Fredsoe, Solution of pore pressure build up due to progressive waves, Int. J. Numer. Anal. Method Geomech. 25 (9) (2001) 885–907.
[38] B.M. Sumer, V.S.O. Kirca, J. Fredsoe, Experimental validation of a mathematical model for seabed liquefaction in waves, in: Proceedings of the International Offshore and Polar Engineering Conference, pp. 1010–1018, 2011.
[39] J. Li, D.S. Jeng, Response of a porous seabed around breakwater heads, Ocean Eng. 35 (8-9) (2008) 864–886.
[40] F. Oka, A. Yashima, T. Shibata, M. Kato, R. Uzuoka, Fem-fdm coupled liquefaction analysis of a porous soil using an elasto-plastic model, Appl. Sci. Res. 52 (3) (1994) 209–245.
[41] Y. Di, T. Sato, Liquefaction analysis of saturated soils taking into account variation in porosity and permeability with large deformation, Comput. Geotech. 30 (7) (2003) 623–635.
[42] S.L. Dunn, P.L. Vun, A.H.C. Chan, J.S. Damgaard, Numerical modeling of wave-induced liquefaction around pipelines, J. Waterw. Port Coastal Ocean Eng. ASCE 132 (4) (2006) 276–288.
[43] S. Sassa, H. Sekiguchi, Analysis of wave-induced liquefaction of sand beds, Géotechnique 51 (2) (2001) 115–126.
[44] S. Sassa, H. Sekiguchi, J. Miyamoto, Analysis of progressive liquefaction as a moving-boundary problem, Géotechnique 51 (10) (2001) 847–857.
[45] M. Pastor, O.C. Zienkiewicz, A.H.C. Chan, Generalized plasticity and the modelling of soil behaviour, Int. J. Numer. Anal. Methods Geomech. 14 (1990) 151–190.
[46] O.C. Zienkiewicz, C.T. Chang, P. Bettess, Drained, undrained, consolidating and dynamic behaviour assumptions in soils, Géotechnique 30 (4) (1980) 385–395.
[47] A.H.C Chan, A unified finite element solution to static and dynamic problems of geomechanics (PhD thesis), University of Wales, Swansea Wales, February 1988.
[48] J.H. Ye, D.-S. Jeng, Effects of bottom shear stresses on the wave-induced dynamic response in a porous seabed: Poro-wssi (shear) model, Acta Mech. Sin. 27 (6) (2011) 898–910.
[49] O.C. Zienkiewicz, A.H.C. Chan, M. Pastor, B.A. Schrefler, T. Shiomi, Computational Geomechanics with Special Reference to Earthquake Engineering, John Wiley and Sons, England, 1999.
[50] M. Pastor, A.H.C. Chan, P. Mira, D. Manzanal, Merodo J.A. Fernndez, T. Blanc, Computational geomechanics: The heritage of olek zienkiewicz, Int. J. Numer. Methods Eng. 87 (1–5) (2011) 457–489.
[51] T.J. Hsu, T. Sakakiyama, P.L.F. Liu, A numerical model for wave motions and turbulence flows in front of a composite breakwater, Coastal Eng. 46 (2002) 25–50.
[52] P.L.F. Liu, P.Z. Lin, K.A. Chang, T. Sakakiyama, Numerical modeling of wave interaction with porous structures, J. Waterw. Port Coastal Ocean Eng. ASCE 125 (1999) 322–330.
[53] J.L. Lara, I.J. Losada, M. Maza, R. Guanche, Breaking solitary wave evolution over a porous underwater step, Coastal Eng. 58 (9) (2011) 837–850.
[54] P. Lin, P.L. F Liu, A numerical study of breaking waves in the surf zone, J. Fluid Mech. 359 (1998) 239–264.

[55] W. Rodi, Turbulence Models and Their Application in Hydraulics-State-of-the-Art Review, IAHR Publication, 1980.
[56] P.Z. Lin, Numerical modeling of breaking waves (PhD thesis), Cornell Universtity, Ithaca N.Y. USA, 1998.
[57] Z.P. Lin, P.L-F. Liu, Internal wave-maker for Navier–Stokes equations models, J. Waterw. Port Coastal Ocean Eng. 99 (4) (1999) 207–215.
[58] J.H. Ye, D.-S. Jeng, R. Wang, C.Q. Zhu, Validation of a 2-D semi-coupled numerical model for fluid–structure–seabed interaction, J. Fluids Struct. 42 (2013) 333–357.
[59] J.H. Ye, Numerical modelling of consolidation of 2-D porous unsaturated seabed under a composite breakwater, Mechanika 18 (4) (2012) 373–379.
[60] J.H. Ye, D.-S. Jeng, A.H C. Chan, Consolidation and dynamics of 3D unsaturated porous seabed under rigid caisson breakwater loaded by hydrostatic pressure and wave, Sci. China Technol. Sci. 55 (8) (2012) 2362–2376.
[61] S. Okusa, Wave-induced stress in unsaturated submarine sediments, Géotechnique 35 (4) (1985) 517–532.
[62] J. H Ye, 3D liquefaction criteria for seabed considering the cohesion and friction of soil, Appl. Ocean Res. 37 (2012) 111–119.
[63] K. Ishihara, Liquefaction and flow failure during earthquakes, Géotechnique 43 (3) (1993) 351–451.
[64] J. Wu, A.M Kammaerer, M.F Riemer, R.B Seed, J.M Pestana. Laboratory study of liquefaction triggering criteria, in: Proceedings of 13th World Conference on Earthquake Engineering, Vancouver, British Columbia, Canada, 2004. Paper No. 2580.
[65] J.Wu, R.B Seed, J.M Pestana, Liquefaction triggering and post liquefaction deformations of monterey 0/30 sand under uni-directional cyclic simple shear loading, Technical report, University of California, Berkeley, 2003. Geotechnical Engineering Research Report No. UCB/GE-2003/01.